Multimodal profiling unveils a reversible basal-like breast cancer cell state resistant to AKT inhibition

Colin D.H. Ratcliffe[1], Hugh Sparks[2], Giulia L.M. Boezio[3], Yuriy Alexandrov[2], Robert P. Jenkins[1], Alix Le Marois[1], Pablo Soro-Barrio[4], Rebecca Lee[1], Stephanie Strohbuecker[4], Sudeep Joshi[5,6], James K. Ellis[7], Anne-Marie Fortier[8], Nils Gustafsson[2], Ana C. Cunha[9], Morag Park[8], James I. MacRae[7], Andrea Serio[5,6,10], James Briscoe[3], Andy Riddell[11], Simon T. Barry[12], Christopher Dunsby[2], Erik Sahai[1]

[1] Tumour Cell Biology Laboratory, The Francis Crick Institute, London, NW1 1AT, UK
[2] Photonics Group, Imperial College London, South Kensington Campus, London, SW7 2AZ, UK
[3] Developmental Dynamics Laboratory, The Francis Crick Institute, London, NW1 1AT, UK
[4] Bioinformatics & Biostatistics, The Francis Crick Institute, London, NW1 1AT, UK
[5] Neural Circuit Bioengineering and Disease Modelling Laboratory, The Francis Crick Institute, London, NW1 1AT, UK
[6] Basic & Clinical Neuroscience Department, Institute of Psychiatry, Psychology and Neuroscience (IoPPN), King's College London, Maurice Wohl Clinical Neuroscience Institute, London, UK
[7] Metabolomics, The Francis Crick Institute, London, NW1 1AT, UK
[8] Goodman Cancer Institute, McGill University, Depts Biochemistry and Oncology, McGill University, Montréal, Canada
[9] Viral Vector Core, The Francis Crick Institute, London, NW1 1AT, UK
[10] Dementia Research Institute (UK DRI), London, United Kingdom
[11] Flow Cytometry, The Francis Crick Institute, London, NW1 1AT, UK
[12] OTD, Early Oncology, AstraZeneca, Cambridge, CB2 0AA, UK

Abstract

The PI3K/AKT/mTOR pathway is central to the control of cellular metabolism and cell growth. However, pharmacological inhibition of the pathway is not uniformly effective across cancer types, or even within a single tumour. In this study, we leverage oblique plane microscopy (OPM) of breast cancer organoids containing molecular biosensors and lineage tracing approaches to uncover a source of heterogeneity in response to AKT inhibition. We find that organoids expressing *KRT14*, a marker of basal cells in the normal breast epithelium, are resistant to AKT inhibition. Furthermore, the master transcription factor of basal cell state, ΔNp63α, is sufficient to confer resistance to AKT kinase inhibition in human triple negative breast cancer (TNBC) organoids. Our studies indicate that cells can transition between cell states within four weeks. This property means that AKT inhibition only delays tumour growth, with fully resistant tumours rich in KRT14+ cells resulting. Thus, resistance to AKT inhibition in TNBC exploits a repertoire of cell states and switching mechanisms inherent to the biology of the breast.

Introduction

Heterogeneity between cancer cells can undermine the efficacy of therapy, with non-genetic and genetic mechanisms generating diversity in cancer cell states. In some cases, resistant cells arise after exposure to therapy, with cells entering a persister cell state prior to transitioning to a resistant state (França et al., 2024; Sharma et al., 2010). In other cases,

tumours contain a subset of cells that are therapy resistant before treatment, despite these mutations being truncal (Beumers et al., 2023; Oren et al., 2021; Russo et al., 2019).

The PI3K pathway is activated in the majority of cancers, with mutations in *PIK3CA*, *AKT*, and *PTEN* observed in over half of all solid tumours, leading to increased glucose uptake as well as increased mTOR, and S6 kinase activity (Fabrice et al., 2019; Juric et al., 2017, 2018; Koboldt et al., 2012; Mayer et al., 2014; Sanchez-Vega et al., 2018). These changes ultimately lead to increased glycolysis and protein synthesis, enabling tumour growth (Bosch et al., 2015; Fruman et al., 2017; Le et al., 2016; Leroy et al., 2016; Simond et al., 2017; Varkaris, Pazolli, et al., 2024; Vasan et al., 2019). The frequent activation of PI3K/AKT signalling in tumours and its central role in cell growth have led to development and clinical implementation of PI3K and AKT inhibitors. Pharmacological inhibition of either PI3K or AKT provides clinical benefit in certain contexts, although durable responses are rare with reactivation of mTOR and S6 kinase frequently observed (Elkabets et al., 2013; Gris-Oliver et al., 2020; Juric et al., 2015; Schmid et al., 2018, 2020; Turner et al., 2019; Varkaris, Fece de la Cruz, et al., 2024).

Intriguingly, not all tumour types with activation of PI3 kinase signalling benefit from therapies that target the pathway. AKT inhibition is a novel strategy in the United Kingdom to treat advanced ESR1+ breast cancer with abnormal *PIK3CA*, *AKT1* or *PTEN* (Turner et al., 2023), but does not provide overall survival benefit in triple-negative disease despite frequent mutational activation of PI3 kinase signalling. Therefore, mutations alone are not sufficient to explain which tumours respond to inhibition of the pathway, nor are they sufficient to explain resistance. Recent work has suggested that tumour regression through Akt inhibition requires adoption of luminal-like features, supporting a role for non-genetic heterogeneity in cell states for resistance to AKT inhibitors (Schade et al., 2024).

Linking heterogeneity in cell state to dynamic changes such as cell signalling, cell metabolism, and ultimately cell fate following therapeutic intervention is challenging. Firstly, conventional cell culture models fail to recapitulate the cell states observed in patients. This can be overcome through the use of patient-derived xenografts and patient-derived organoids (Drost & Clevers, 2018; Grasset et al., 2025; Guillen et al., 2022; Krieger et al., 2021; LeSavage et al., 2022; Roerink et al., 2018). Secondly, the majority of single-cell analysis technologies used to study inter-cellular variation are destructive, hence are not able to capture a cell's history or future trajectory. Barcoding and lineage tracing strategies have been developed to overcome this problem, but these still struggle to capture the spatial context of cells (Goyal et al., 2023; Weinreb et al., 2020). Live imaging approaches are well-suited to recording longitudinal data before and after therapeutic challenge and the spatial context of cells, with biosensors being deployed to reveal information about cell signalling and state (Conway et al., 2018; Hirata et al., 2015; Kondo et al., 2021; Le Marois et al., 2024; Madsen et al., 2018; Nguyen et al., 2025; Ponsioen et al., 2021; Sparks et al., 2018). The advent of light-sheet imaging has transformed our ability to image three-dimensional models that closely recapitulate the biology of tumours, such as organoids and tissue explants. In particular, the development of light-sheet fluorescence microscope systems is beginning to enable large numbers of 3D structures to be imaged in parallel (Beghin et al., 2022; de Medeiros et al., 2022; Maioli et al., 2016).

We leverage several complementary experimental approaches to address the resistance of triple-negative breast cancer (TNBC) to AKT inhibition in organoid and *in vivo* models. These analyses identify a subset of TNBC organoids that exhibit a signature positive for KRT14, a marker of basal cells in the normal breast, that resist a bottleneck selection pressure imposed by AKT inhibition. The resistant cell state is reversible and can be driven by ΔNp63α overexpression. Therefore, we propose that resistance to AKT inhibition in TNBC

exploits a repertoire of cell states and reversible switching mechanisms inherent to the biology of the breast.

Results

Recapitulation of heterogeneous breast tumour cell states

To investigate the phenotypic heterogeneity of triple negative breast cancer, we employed patient-derived xenograft organoids (PDXOs). GCRC1915, recapitulates histological and molecular features frequently observed in TNBC, including genetic alterations such as *TP53* mutation, gain of *PIK3CA* and low expression of PTEN (Savage et al., 2020). The heterogeneity of cell states in organoids and transitions between them was interrogated by combined single-cell sequencing with the LARRY barcode labelling strategy (Weinreb et al., 2020). For brevity, we termed this framework **L**arry **B**arcoding **E**xpansion and **T**reatment with **O**rganoid **S**orting and **S**equencing (LBETROSS) (Supplemental Figure 1a). GCRC1915 organoids were dissociated, single cells transduced with lentivirus that expressed GFP with a barcode in the 3' UTR sequence, seeded as single cells and grown for 7 days to allow organoid regrowth. GFP+ organoids were enriched and ultimately sequenced.

To apply this approach in tumours we made use of a custom-built organoid sampling platform coupled to live-cell microscopy, termed VISIBLE for GFP+ organoid enrichment, and then injected these into mice, where tumours formed and were harvested (Supplemental Figure 1a – left branch) (Joshi et al., 2025). Dissociated human cells were then processed for single-cell RNA sequencing and analysed. To assess how this model might relate to human breast cancer, we mapped onto this dataset 7 single-cell gene modules (GMs) previously described in a human breast cancer single-cell atlas (Wu et al., 2021). Distinct UMAP regions enriched for GM1, 2, 3, 6 and 7, and to a lesser extent GM4, were identifiable (Supplementary Figure 1b). Unsupervised cluster detection identified 3 cell clusters (Clusters I, II and III) that were enriched for specific gene modules, demonstrating that this model recapitulates gene expression profiles previously observed in human patients and encompasses heterogeneous phenotypic space to interrogate clonal dynamics (Figure 1a & Supplementary Figure 1c).

We performed lineage analysis of cells expressing the ectopic GFP transcript that includes a unique barcode. Barcodes were detected in 5% of cells and 60 clonal groups with 4 or more cells were identified (Figure 1b). Intriguingly, clonal groups were scattered between clusters with binomial testing revealing that 95% of these were present in multiple clusters, supporting that this model recapitulates non-genetic phenotypic heterogeneity that is a feature of TNBC (Figure 1c & d). These data also indicate that cells transition between phenotypic states within a six-week timeframe.

Non-genetic heterogeneity in response to AKT inhibition

Next, we investigated the relevance of this pre-existing heterogeneity on treatment response. Endpoint assays have recently been used to interrogate drug response in TNBC organoids (Guillen et al., 2022), however, we rationalised that treating them with varying concentrations of the Akt inhibitor, Capivasertib, for 4 days and performing timelapse imaging would be informative. We used a pre-trained neural network for object identification, followed by tracking, to derive growth rates for individual organoids (Ershov et al., 2022; Pachitariu & Stringer, 2022). For comparison, we treated the organoids with three other classes of cancer therapy; the microtubule stabiliser Paclitaxel, the platinum-based Cisplatin and the CDK4/6 inhibitor Palbociclib. Resistance to Cisplatin, observed in the GCRC1915 PDX (Savage et al., 2020), was recapitulated by the organoid model, along with sensitivity to Paclitaxel. The organoids were also sensitive to Palbociclib. Intriguingly, Figure 1d shows that response to Capivasertib diverged from those of the other cytotoxic drugs. In particular, the Capivasertib dose-response had a shallower slope and there was a greater proportion of organoids that

maintained a moderate growth rate even at high doses of the drug. This heterogeneity was clearly evident in the timelapse movies, with some organoids continuing to grow while others of similar size and in the same field of view did not (Figure 1f, Supplemental Figure 2a and Supplemental Movie 1). Comparable results were obtained with the AKT inhibitor Ipatasertib, indicating that the variable response is not specific to Capivasertib (Supplemental Figure 2a, b & c). Analysis of PI3K inhibitors, an mTOR inhibitor, and a Cytohesin inhibitor suggested that PIK3CA was likely to be the key isoform acting upstream of AKT, and that mTOR was a critical downstream effector (Supplemental Figure 2d).

The heterogeneity in response to AKTi suggested that there may be a pre-existing resistant population of cells within the PDXO culture. To explore if this might be underpinned by a genetic subclone within GCRC1915, we isolated single cell-derived sub-lines of the PDXO (Figure 1g). A power calculation based on the proportion of organoids that continued growing in the presence of Capivasertib indicated that 18 sub-lines would be sufficient to determine if a pre-existing resistant sub-clone was present with a significance level of <0.05. The sub-lines were then tested for their response to Capivasertib. Of note, all 18 sub-lines of GCRC1915 were sensitive to Capivasertib and none grew in the presence of Capivasertib at the same rate as DMSO-treated controls, arguing against a genetic or at least phenotypically stable population of cells resistant to AKT inhibition (Figure 1h).

Simultaneous evaluation of AKT activity, glucose metabolism, and organoid growth

The failure to respond to a therapy could reflect ineffective inhibition of the target, the lack of coupling between the target and key biological processes, or the lack of dependence of the resistant cells on the biological process regulated by the drug target. We sought to resolve these differing scenarios by measuring both single-cell AKT activity and glucose metabolism, along with whole-organoid features. We leveraged a custom-built dual-view oblique plane microscope (dOPM) to perform multi-dimensional live-cell imaging compatible with a multi-well plate format (Figure 2a). GCRC1915 organoids were transduced using a piggyBac system to express a modified segment of the AKT substrate FOXO1 ($FOXO1_{10A3D}$-mRuby2) that accumulates in the cytoplasm when phosphorylated (Gross et al., 2019), a glucose biosensor that reports on glycolysis (Kondo et al., 2021; Takanaga et al., 2008), and a nuclear label for image processing purposes (Oliinyk et al., 2019) (Figure 2b & c). A bespoke pipeline was set up to analyse AKT activity and glucose levels in every cell of every organoid (Figure 2d). Individual organoids were assigned a unique identity, and all cell metrics were linked to the organoid identity (Figure 2e). Within the organoids, nuclei were segmented in 3D based on the H2B-miRFP670nano signal. This was used to generate both a nuclear mask and a perinuclear mask, encompassing a one-micron thick shell immediately outside the nucleus. This enabled us to determine the number of nuclei per organoid and derive an organoid growth metric. AKT activity was determined by dividing the $FOXO1_{10A3D}$-mRuby2 signal in the perinuclear mask by the sum of the nuclear mask and the perinuclear mask, with higher values indicating greater AKT activity. Intracellular glucose levels were determined by ratiometric analysis of the Citrine sensitised emission and eCFP signals. Control experiments using Koningic acid and glucose-free media confirmed the fidelity of the glucose sensor, and additionally revealed an up-regulation of AKT activity when glucose was absent (Supplemental Figure 3a). Thus, we established methodology enabling direct *in situ* assessment of drug efficacy, the coupling of AKT to glycolysis, and organoid growth at scale.

Differential dynamics of AKT regulation and coupling to glucose distinguish organoids resistant to AKT inhibition

GRC1915 organoids were imaged immediately prior to the administration of drug, 24 hours later, and 96 hours later. Figure 2e shows 50 representative DMSO and Capivasertib-treated organoids from one of 4 experimental replicates. As described above, metrics were

determined for every segmented nucleus, with each cell being assigned to a specific organoid. Principal Component Analysis (PCA) incorporating both biosensor and morphological metrics were used to explore the diversity of cell states in the organoids. Figure 2f shows changing cell metrics upon treatment. Cells treated with Koningic acid showed uniform changes. In contrast, Capivasertib-treated cells showed divergent responses with two distinct populations emerging at 96 hours. A similar divergence was observed when the response to Capivasertib was analysed at the organoid level, suggesting the majority of cells within an organoid respond in a similar manner to the drug (Figure 2g). Figure 2h confirms that cell states in any given organoid group together 96 hours after drug treatment. Thus, our imaging platform reveals divergence in response to AKT inhibition at the organoid level.

We next interrogated how organoid metrics relate to their growth rate. Overlaying the growth rates indicated that the cluster containing the majority of the control organoids had a high growth rate, while the Capivasertib-treated organoids were split between the high growth rate cluster and a low growth rate cluster, thus confirming the analysis in Figure 1 (Supplemental Figure 3a). To gain further insights, we investigated correlations between metrics and replotted the data (Figure 3a). Here, each column represents an organoid, and the columns are ranked based on growth rate (shown in the upper panel). The central and lower panels indicate the glucose sensor FRET signal and AKT activity at 96 hours, respectively. Every cell in an organoid is represented as a thin horizontal bar contributing to the height of the column, with taller columns indicating more cells in the organoid, and the cells are ranked in order of increasing glucose sensor FRET signal. These analyses reveal multiple aspects of the relationship between AKT, glucose levels, and growth in the presence or absence of AKT inhibition (Figure 3b).

Firstly, control DMSO-treated organoids with higher baseline AKT signalling and glucose levels grew slightly faster (Figure 3a). As expected, AKT inhibition reduced AKT activity and median glucose levels in organoids (Supplemental Figure 4a & b). Moreover, consistent with the premise that all cells within an organoid respond similarly, the standard deviation of the glucose FRET signal across all cells (DMSO-0.6864 and Capivasertib-0.8016) was greater than that within organoids (DMSO-0.4856 and Capivasertib-0.4560). However, not all organoids responded in the same way, with the fastest 15% Capivasertib-treated organoids in our dataset continuing to grow faster than the DMSO median (0.018 1/hour), and these maintained their glucose levels (Figure 3a.vi – note colour uniformity of columns).

The growth rate following AKT inhibition did not correlate with the magnitude of reduction in AKT activity in the 24 hours after drug treatment (Figure 3b & c). Therefore, the heterogeneity in organoid response is not due to some variability in the initial ability of Capivasertib to inhibit its target. Pre-treatment features of the organoids, such as glucose levels or size, did not predict coupling between AKT signalling and resistance (Supplemental Figure 4c & d). However, there was a subtle, but statistically significant, relationship between the growth rate following AKT inhibition and the change in glucose sensor signal (Supplemental Figure 4e). This suggests that a subset of organoids has slightly weaker coupling between AKT activity and glucose levels.

Our longitudinal tracking of organoids to 96 hours enabled us to explore whether the durability of response to Capivasertib varied between organoids, and if this related to the efficacy of the drug in stopping organoid growth. Organoids that showed an increase in AKT activity between 24 - 96 hours had an increase in glucose levels during the same time window (Figure 3d). Crucially, these were the organoids that continued to grow in the presence of drug (Figure 3e). These data establish a clear link between heterogeneity in the durability of AKT inhibition and the downstream consequences of glucose regulation and cell growth. Moreover,

because the organoids shared common media, we can exclude the possibility of differences in drug exposure. These data argue for inter-organoid heterogeneity in the wiring of AKT signalling feedback, with AKTi resistant organoids having a faster restoration of glucose levels following AKT inhibition.

Drug refractory organoids arise from pre-existing cells in a basal state

The diversity in the dependency of glucose levels on AKT in our model might reflect heterogeneity in cell state. Therefore, we sought to obtain a better understanding of the diversity of cell states both between organoids and within organoids. To this end, we leveraged the LBETROSS pipeline (Supplemental Figure 1a – right branch). Organoids were dissociated, single cells transduced with lentivirus that expressed GFP with a barcode in the 3' UTR sequence, seeded as single cells and grown for 3 days. The organoids were then grown in the presence of either DMSO or Capivasertib for 4 days, and the resulting intact organoids were sorted for GFP expression (Supplemental Figure 5a, b and c). Flow cell imaging and subsequent size analysis confirmed our ability to sort organoids from both DMSO and Capivasertib-treated conditions and fluorescently labelled subsets (Supplemental Figure 5d). Subsequently, we analysed single cells by RNA sequencing.

UMAP analysis of 6623 cells revealed three major clusters, numbered 1-3, and two minor clusters, numbered 4 & 5 (Figure 4a). All clusters were represented in both the control DMSO and Capivasertib-treated conditions, indicating that the cell states resistant to the drug are present in the drug naïve context (Figure 4b). No single marker perfectly delineated the different clusters. For example, *KRT14* is higher in cluster 2 and 3, but also present in a subset of cluster 1 and 5 cells, whereas *SOX2* only delineated a subset of cluster 2 cells (Figure 4c). However, analysis of cell cycle phase revealed that clusters 1, 4, and 5 had a higher proportion of cells in G1 following AKT inhibition, whereas clusters 2 and 3 did not (Figure 4d). Additionally, clusters 2 and 3 made up an increased proportion of total cells under Capivasertib-treated conditions, supporting a model where clusters 2 and 3 represent drug-resistant populations. Of note, these clusters were enriched for genes associated with basal-like breast cancer and mammary stem cells, including *SOX2, CD44, KRT14, KRT5* and *TP63* (Figure 4c).

The LBETROSS pipeline enables lineage analysis of cells and, consequently, the identification of cell states that contribute to the make-up of a given organoid. Barcodes could be detected in 37 to 54% of cells. A mean of 314 clonal identities could be detected per sample, with clone sizes ranging from 1 to 29 cells and an average of about 2 to 3 cells within each clonal group. A model favouring higher inter-organoid heterogeneity would be supported if cells from a given clonal barcode or organoid would predominantly map within one cluster. We restricted our analysis to clonal groups that contained at least 4 cells. Figure 4e shows the five largest clonal groups from each condition overlayed onto UMAP space where we find that differences in gene expression within a given organoid is limited, with almost no barcodes being present in more than one cluster. Indeed, single cluster-contained clonal groups are the three most common distributions of clonal groups amongst gene expression clusters and binomial testing reveals that >96% of clonal groups confidently belong to a single cluster (Figure 4f & g). These data enable us to determine that switching between clusters requires more than seven days, which is the time between barcode introduction and transcriptomic analysis.

Together, these data support the idea that inter-organoid heterogeneity arises from the heterogeneity in the state of the individual cells that seed the organoid; for example, some are more basal and other more luminal, with the former being resistant to AKT inhibition. Within the time frame of the experiment, cells do not transition between states and, therefore, all cells

within an organoid are in a similar state and show a similar response to AKT inhibition. Thus, intra-organoid heterogeneity in drug response is much less than inter-organoid heterogeneity.

Long-term resistance to AKT inhibition is linked to a basal cell state

We set out to determine if the traits associated with short-term AKTi resistance were similar to those in organoids exposed to drug for many weeks. Organoids were treated and passaged with Capivasertib for four weeks to generate a population of uniformly resistant organoids (Figure 5a). Metabolomic characterisation confirmed that AKT inhibition had a greatly reduced impact on glucose-derived pyruvate and lactate in the resistant organoids (Supplemental Figure 6). These organoids also had increased glucose-derived ^{13}C into the TCA cycle intermediates citrate, glutamate, fumarate, aspartate and malate. These data are consistent with data in Figure 2, showing that the organoids capable of growth in the presence of Capivasertib have maintained their glucose levels. Similarly, the resistant organoids had slightly elevated levels of pS6 compared to parental organoids in the presence of Capivasertib (Supplemental Figure 7a). However, the organoids had not entered a broadly drug-resistant cell state since sensitivity to Paclitaxel was not affected (Supplemental Figure 7b & c).

Data presented thus far support a model where resistance to Capivasertib is driven by cell states underpinned by inter-organoid heterogeneity. Crucially, cessation of Capivasertib treatment led to a reversion to drug sensitivity within 4-6 weeks, further emphasising the non-genetic nature of the AKTi-resistant state (Figure 5a).

The long-term Capivasertib-resistant organoids were next analysed by bulk RNA sequencing (Figure 5b), and the results were cross-referenced with the single-cell RNA sequencing (Figure 5c). There was a highly significant overlap between the genes up-regulated in resistant cell populations after 4 days and long-term drug treatment (Figure 5d). Moreover, the genes up-regulated in the long-term drug-treated cells mapped to clusters 2 and 3 identified by LBETROSS. Analysis of genes concordantly regulated in both data sets revealed that resistant cells had a transcription profile with strong similarity to basal cells of the breast, notably high expression of *SOX2*, *KRT5*, *KRT14*, and *ITGA6* (Figure 5e).

OPM imaging-based analysis confirmed that resistant organoids were highly enriched for KRT14 and that this state was reversible since Capivasertib-rested organoids appeared more similar to parental. There was no difference in organoid size between DMSO, resistant or capivasertib-rested organoids (Supplemental Figure 7d). KRT14 staining in DMSO-treated conditions also did not associate with organoid size, suggesting that both KRT14- and KRT14+ organoids are capable of growing and contributing to the population under standard growth conditions (Supplemental Figure 7e). Higher levels of ITGA6 and KRT14 in resistant organoids were confirmed by flow cytometry, with lower levels of EPCAM observed in resistant organoids (Supplemental Figure 7f, g & h). Re-emergence of a ITGA6 low population occurred at 3 weeks after removal of Capivasertib from resistant organoids (Supplemental Figure 7i) and rested organoids displayed ITGA6, KRT14, and EPCAM levels similar to drug naïve organoids, confirming the reversibility of the resistant phenotype.

Having established that AKT inhibition selects for cells in a basal state, we sought to test if cells in a basal state were intrinsically resistant to AKT inhibition. Drug-naïve cells in more basal states were sorted on the basis of ITGA6 expression and subjected to AKT inhibition. Supplemental Figure 7j shows that ITGA6 high basal drug-naïve cells are enriched for cells that grow under AKT inhibition, whereas ITGA6 low luminal cells were predominantly drug sensitive. Altogether, these data support a model whereby a pre-existing cell state with features of normal breast basal cells is resistant to AKT kinase inhibition.

ΔNp63 is sufficient to confer resistance to AKT inhibition

We sought to identify the critical cell state regulators driving the transition into the basal drug resistant state. Using ChEA3, we compared transcription factor targets and genes enriched in Capivasertib-resistant organoids that overlapped with either cluster 2 or 3 from the LBETROSS (Keenan et al., 2019). This revealed a strong overlap with TP63 target genes. The transcription factor ΔNp63α is an established regulator of the basal cell lineage in the mammary gland (Wuidart et al., 2018). Overexpression of ΔNp63α, promoted elevated expression of basal cell markers ITGA6 and KRT14 and reduced levels of EPCAM, whereas the effect was comparatively more attenuated when overexpressing a DNA-binding domain mutant (R304W) (Supplemental Figure 7k, l, m, n). More strikingly, ΔNp63α overexpression also rendered organoids insensitive to Capivasertib, whereas organoids expressing the R304W mutant were not (Figure 5g). Thus, the drug resistant state arises as a result of the endogenous program that determines basal cell identity.

A basal-like cell state is enriched in Capivasertib-treated tumours

To directly test whether a Capivasertib-resistant state might make up a significant portion of a pre-established tumour we used a 106-gene signature, which we name CaRe63, made up of ΔNp63α targets that were upregulated in Capivasertib-resistant organoids. We interrogated our scRNA sequencing dataset of LARRY-labelled tumours with this approach and identified a subpopulation of cells that mapped to Cluster II and another that mapped to Cluster III, which was also characterised by upregulation of KRT14 expression (Figure 6a and b). Gene set enrichment analysis of Cluster III markers identified gene sets for basal-like breast cancer, many of which were also identified in Capivasertib-resistant clusters *in vitro* (Figure 6c). Therefore, multiple pre-existing cell states might provide the phenotypic landscape required for a tumour to quickly escape therapeutic intervention.

To test this hypothesis, we generated vehicle-treated and Capivasertib-resistant tumours (Figure 6d and e). Capivasertib significantly impaired tumour growth, however the tumour endpoint was only delayed and endpoint was reached 3 weeks after vehicle control tumours. Multiplexed immunostaining confirmed the presence of heterogeneous cell states in control tumours. Concordant with scRNA sequencing analysis, control tumours contained a mixture of KRT14 positive and negative cells (Figure 6f). KRT14 positive cells were typically located near laminin, which denoted blood vessels and the edge of tumour cell nests. These KRT14 positive cells had higher pS6 and Ki67 staining indicating that they are likely to be responsible for continued tumour growth. Capivasertib-treated tumours exhibited less heterogeneity and were dominated by KRT14 positive cells (Figure 6g). Although we observed a decrease in phospho-S6 levels following AKT inhibition, it was above the levels in KRT14 negative cells in control tumours and Ki67 levels were maintained (Figure 6h), suggesting sufficient pathway activity for cell growth. Interestingly, KRT14 positive cells were no longer confined to regions surrounding laminin staining but were uniformly distributed. These data establish that within 2-3 weeks Capivasertib treatment leads to the dominance of more basal KRT14 positive breast cancer cells.

Finally, we sought to relate our observations to patient data. We used the CaRe63 signature to interrogate both inter-patient and intra-patient heterogeneity amongst human breast cancer described in Wu et al. Figure 6i, shows that some patients were uniformly low for CaRe63 (CID4495 & CID44971), while others exhibited intra-tumour heterogeneity similar to that observed in our experiments (CID4513, CID4515 & CID4523). We propose that the former patients would benefit from Capivasertib, while the latter would not. Together, these analyses demonstrate that AKT inhibitor resistance is linked to the inherent biology of the breast, with basal cells exhibiting reduced coupling of AKT to S6 and regulation of glycolysis (Figure 6j).

Discussion

The high frequency of mutations in *PI3K* isoforms, *PTEN*, and *AKT* make the pathway an attractive target for therapeutic intervention. However, not all tumours respond and responses are not always durable. Phase III clinical trials demonstrated overall efficacy of AKT inhibition using Capivasertib in ER+ disease, but not TNBC. Using a 3D culture system of human TNBC organoids we have uncovered a non-genetic resistant cell state driven by ΔNp63α. We have used orthogonal approaches including a modified Luria-Delbruck assay, LBETROSS, metabolomics and more conventional molecular biology techniques. However, live imaging has the key advantage of being non-destructive and enabling varying cell states to be unambiguously and directly linked to different cell fates, such as cell proliferation or cell death. Capturing the intra-tumour heterogeneity recapitulated by 3D organoids requires microscopes with high resolution in all spatial dimensions that can operate at light levels that are not damaging to cells. In principle, conventional light-sheet microscopy is well suited for organoid imaging, but the requirement for orthogonal objectives makes sample preparation and mounting very challenging, especially if many hundreds of organoids are to be imaged in parallel. Therefore, technological limitations may restrict lines of inquiry relating to biological variability in therapeutic responses. To overcome this challenge, we implemented dual-view OPM that uses only a single objective and is compatible with a wide range of multi-well plate formats enabling multi-channel imaging of organoids structures up to ~200 µm in size. In this work, we have imaged 1530 organoids with single-cell resolution across conditions that included both live cell and fixed cells. This throughput allowed us to understand a subset of TNBC organoids that are refractory to AKT inhibition.

The observed resistant state exhibited poor coupling between glucose metabolism with AKT activity and these organoids exhibited enhanced shunting of glucose-derived carbon to citric acid cycle intermediates. This cell state is likely to pre-exist in many TNBC cases and our analysis indicates that cells can transition in and out of this state on a timescale of between one and four weeks (Cheung et al., 2013; Khalil et al., 2024). Over time, epigenetic modifiers may drive TNBC cells towards what are normally rare or sporadic cell states that, when combined with AKT inhibition, trigger a cell death program with similarities to involution (Marsolier et al., 2022; Schade et al., 2024). Together, this may reflect differing requirements for extracellular cues in secretory luminal cells or contractile basal cells. Supporting this hypothesis, different metabolic sensitivities have been described for the normal breast epithelial cell subtypes, suggesting that normal epithelial programs are contributing to resistance to Akt inhibition in what has been described to be a heterogeneous tumour type (Mahendralingam et al., 2021). In our model, this was recapitulated by the observed inter-organoid heterogeneity. Hence, this work offers an explanation for the differing success of AKT inhibition in ER+ breast cancer, which is more luminal in its cell states, and TNBC, which exhibits basal-like characteristics.

Acknowledgements

The authors would like to acknowledge all members of the Sahai laboratory for their insightful comments. We thank the Cell Sciences, Flow Cytometry, Advanced Light Microscopy, Genomics, Bioinformatics and Biostatistics, Experimental Histopathology, High Throughput Screening, Human Biology Facility, Biological Research facility and Research Illustration teams from the Francis Crick Institute for their assistance and training. **C.D.H.R.** is a recipient of a Bourse postdoctorale from the Fonds de recherche du Québec – Santé (https://doi.org/10.69777/273104), as well as a EACR-AstraZeneca Postdoctoral Fellowship. **C.D.H.R.** is supported by funding from the AstraZeneca-Crick Research Alliance. **G.L.M.B.** is supported by an EMBO postdoctoral fellowship (ALTF-792-2021). **S.J.** acknowledges funding support from the BBSRC TRDF Grant (BB/T011572/1) and Chris Banton Fund of The Francis Crick Institute, London. **S.J.** thanks MedTech Super Connector (MTSC) fellowship and BBSRC ICURe Explore Programme for funding support towards commercialization of innovation. **S.J.** is the recipient of the LUSH Prize in the young researcher category. **J.B.** is supported by the European Research Council under European Union (EU) Horizon 2020 research and innovation program grant 742138 and by the Wellcome Trust (220379/D/20/Z) **C.D.** is supported by EPSRC (EP/T003103/1), CRUK Accelerator (C10441/A29368) and Imperial EPSRC Impact Acceleration Account (EP/R511547/1) **E.S.** is supported by the Francis Crick Institute, which receives its core funding from Cancer Research UK (CC2040), the UK Medical Research Council (CC2040), and the Wellcome Trust (CC2040) and the European Research Council (ERC Advanced Grant CAN_ORGANISE, Grant agreement number 101019366). The breast cancer patient-derived xenograft organoids PDXO GCRC1915 was obtained from the breast tissue and data bank (Park lab, McGill University) (PMID: 32546838), supported by the Réseau de Recherche sur le Cancer of the Fonds de Recherche du Québec-Santé and the Québec Breast Cancer Foundation, and certified by the Canadian Tumor Repository Network (CTRNet). The work was supported by a CRUK Accelerator award (MACH3CANCER, A29386) and the dOPM instrument was initially developed under a project funded by the EPSRC (EP/T003103/1).

Materials and methods

Organoid lines, plasmids and compounds

GCRC1915 PDXO parental organoid lines were generated from the GCRC1915Tc PDX (Savage et al.). Organoids were routinely cultured in 12-well dishes pre-coated with a 150 µL layer of Cultrex RGF Basement Membrane Extract, type 2, PathClear®. Organoids were maintained (37°C, 5% CO_2, humidified atmosphere) in culture media consisting of Advanced DMEM/F12 (Cat# 12634-010, Invitrogen), 1X GlutaMAX (Cat# 35050-061, Gibco), 10mM HEPES (Cat# 5630-080, Gibco), 1% Penicillin-Streptomycin (Cat# 15140-122, Gibco), 1X B-27 supplement (Cat# 17504044, Life tech), 0.1X mNoggin Conditioned Media (5X Concentrate obtained from Cell Services Platform at the Francis Crick Institute), 0.1X R-spondin-1 conditioned media (5X Concentrate obtained from Cell Services Platform at the Francis Crick Institute), 5 ng/mL human recombinant EGF (Cat# 78006.1, StemCell), 5 ng/mL human recombinant FGF-7 (KGF) (Cat# 78046, StemCell), 20 ng/mL human recombinant FGF-10 (KGF) (Cat# 78037.1, StemCell), 5 nM Neuregulin 1 (Cat# 78071.1, StemCell), 500 nM A83-01 (Cat# 2939/10, Tocris), 500 nM SB202190 (Cat# S7067, Sigma), 1.25 mM N-acetylcysteine (Cat# A9165, Sigma), 5 mM Nicotinamide (Cat# N0636, Sigma), 10 µM Y-27632 (Cat# 1254/1, Biotechne) and 5% Cultrex RGF Basement Membrane Extract, type 2, PathClear® (Cat# 3533-010-02, R&D Systems). Media was changed every 3 or 4 days and organoids were passaged once per week. For passaging, organoids were first treated with 1mg/mL collagenase/dispase diluted in resuspension media (DMEM/F12 (Cat# 11320033, Gibco) with 1% FBS and 1% Penicillin-Streptomycin (Cat# 15140-122, Gibco)) for 90 minutes. Then, organoids were resuspended in accutase for 10 minutes at room temperature, followed by 10 minutes at 37°C to obtain a single-cell suspension. Cells were pelleted, resuspended in resuspension media, counted and 1-2 x 10^5 were plated in growth media. All organoid lines were authenticated and tested for mycoplasma contamination by the Cell Services Platform at the Francis Crick Institute. Clonal organoid lines were generated by single-cell sorting into 96-well v-bottom Cell-repellent plates (Cat#61970, Greiner Bio-One GmbH) followed by passaging after 2 weeks and expansion. Resistant organoid lines were generated by culturing organoids in the presence of 1 µM Capivasertib (Cat# HY-15431, Insight Biotechnology) for at least 1 month. The corresponding rested line was cultured without Capivasertib for 1-2 months.

Compound Table

Name	Company	Catalog number
Doxorubicin	Sigma	D1515
Cisplatin	Selleckchem	S1166-sel
Paclitaxel	Selleckchem	S1150
Capivasertib	Cambridge Bioscience	15406
Capivasertib (*for in vivo use*)	AstraZeneca	
Palbociclib	Cambridge Bioscience	16273
Alpelisib	Selleckchem	S2814
GSK26366771	Cambridge Bioscience	17380

AZD8186	Cambridge Bioscience	17384
CAL101	Cambridge Bioscience	15279
Buparlisib	Cambridge Bioscience	11587
Pictilisib	Selleckchem	S1065
Ipatasertib	Cambridge Bioscience	18412
MK-2206	Cambridge Bioscience	11593
Everolimus	Cambridge Bioscience	11597
SecinH3	Cambridge Bioscience	100009570
Koningic Acid	Abcam	Ab144269

Primers

PB_5_H2B_F	tgtgctgtctcatcattttggcaaagaattcggcatgccagagccagcgaagtctgctc
P2A_miRFP670_R	aggcccggggttttcttcaacatcacctgcttgctttagcagagagaagtttgtggcgccgctgccgctctgctggatggcgatgcccacc
P2A_FoxO1_F	gttgaagaaaaccccgggcctatggcagaggctccccagg
MglB_T2A_R	agtatcagccatTGGGCCGGGATTTTCCTC
T2A_MglB_F2	aaatcccggcccaATGGCTGATACTCGCATTG
MglB_R	aatcaaatcgccttgaataatgccg
MglB_F	cggcattattcaaggcgatttgatt
PB_YFP_R	GAGGGAAACCGTTGCTAGCTTAAGTTAGTTAACaagcttttacttgtacagctcgtccat
PB_dNp63a_F1	TgtgctgtctcatcattttggcaaagaattcggcATGTTGTACCTGGAAAACAATGCCCAG
PB_dNp63a_R1	GAGGGAAACCGTTGCTAGCTTAAGTTAGTTAAC TCACTCCCCCTCCTCTTTGA
p63_R304W_F1	CTTTGAGGCCTGGATCTGTG
P63_R304W_R1	CACAGATCCAGGCCTCAAAG

Stable organoid lines were generated using the piggybac transposon system. A 1:1 mix of relevant and pBase plasmids (4 µg total DNA) and 12 µL Lipo2000 were incubated for 5 minutes and then added to 0.5 x 10^5 resuspended cells. This mix was incubated (37°C, 5% CO_2, humidified atmosphere) in an ultra-low adherent plate (Cat#10154431, VWR) for 1-4 hours and then replated under standard conditions. After 4 days, media was changed and organoids were selected and continuously cultured with 5 µg/mL blasticidin.

Constructs H2B-miRFP670nano (Cat# 127438 , Addgene), pSBbi-FoxO1_1R_10A_3D (Cat# 106278, Addgene) and ΔNp63α were kind gifts from Vladislav Verkhusha, Laura Heiser and

Karen Vousden respectively. eCFP-MglB-Citrine was described previously. The polycistronic (H2B-miRFP670nano-P2A-FoxO1_1R_10A_3D-T2A-eCFP-MglB-Citrine), mEmerald, ΔNp63α and ΔNp63α (R304W) expressing vectors was generated using PCR amplified fragments and cloned into EcoR1-HF and Hpa1 digested piggybac transposon vector by Gibson Assembly (NEB). All constructs were sequence verified before use.

In vivo experiments

The Francis Crick Institute's Animal Welfare and Ethical Review Body and UK Home Office authority provided by Project License 0736231 approved all animal model procedures. Procedures described in this study were compliant with relevant ethical regulations regarding animal research. For drug studies, Capivasertib was formulated once weekly as a solution in 10% DMSO, 25% Kleptose and dosed twice daily (BID) 8 hours apart by oral gavage 0.1 mL/10g of the animal using a schedule of 4 days dosing, 3 days not dosing at 130 mg/kg. Control animals were dosed with vehicle equivalent to compound dosing groups.

Organoid Lineage tracing

LARRY library amplification

LARRY Barcode Version 1 library was a gift from Fernando Camargo (Addgene #140024). 20 ng of the LARRY plasmid library was transformed into 12 vials (25 µL each) of Stbl4 ElectroMAX cells (ThermoFisher, 11635018). Following 1-hour recovery at 37°C in SOC medium, each bacterial tube was plated onto two 20 × 20 cm agar plates. The next day, cells were rinsed 3 times from plates into a total of 1.5 L of LB, cultured for 2.5 hours at 37°C, and purified using the NucleoBond Xtra Maxi EF (Macherey Nagel, 740424.50). The final DNA yield was 1–1.5 mg.

Lentivirus production

Lentiviral particles were produced using a third-generation lentivirus packaging system: pLP1 (Invitrogen, A43237), pLP2 (Invitrogen, A43237) and pVSV-G (System Biosciences). LARRY library and packaging plasmids were transfected into HEK293T, cells using Lipofectamine 2000 (Invitrogen, 11668500). HEK 293T cells were grown in Dulbecco's modified Eagle's medium (DMEM) (Sigma, D5796) supplemented with 10% foetal bovine serum (FBS) (Biosera, FB-1001/500) and 1% penicillin/streptomycin (Gibco, 15140-122) and transfected in Opti-MEM I (Gibco, 31985). Sixteen hours after transfection, media was replaced with Dulbecco's modified Eagle's medium (DMEM) (Sigma, D5796) supplemented with 10% fetal bovine serum (FBS) (Biosera, FB-1001/500) and 1% penicillin streptomycin (Gibco, 15140-122). 36 and 60 hours after transfection, media were collected, passed through a 0.45 µM filter (Millex-HV Millipore, SLHV033RS), and then ultracentrifuged at 22,000 rpm for 1.5 hours. Pellets were resuspended in sterile Dulbecco's phosphate-buffered saline (DPBS) (Gibco, 14190) and stored at −80 °C.

Plasmid and lentivirus library diversity assessment

For plasmid library sequencing, primers pLARRYfw (TCGTCGGCAGCGTCAGATGTGTATAAGAGACAGaggaaaggacagtgggagtg) and pLARRYrv (GTCTCGTGGGCTCGGAGATGTGTATAAGAGACAGcaaagaccccaacgagaagc) were used to amplify the plasmid library. For lentiviral library sequencing, RNA was extracted from 40 µL of the viral preparation using the Virus NucleoSpin Kit (Macherey Nagel, 740983.50), eluted in 40 µL. 3 µg of RNA were retrotranscribed to cDNA with Superscript VILO (random primers, ThermoFisher 11754050). Amplification was performed with primers

vLARRYfw (TCGTCGGCAGCGTCAGATGTGTATAAGAGACAGaatcctccccccttgctgtcc) and vLARRYrv (GTCTCGTGGGCTCGGAGATGTGTATAAGAGACAGaccgttgctaggagagaccata.

In both cases, mock qPCR was used to determine the minimum cycles to avoid saturation. PCR amplification was then conducted with Q5 High-Fidelity Polymerase (NEB, M0494) using the following conditions: 98°C for 30 s; [98°C for 10 s, 63°C for 30 s, 72°C for 20 s] x 7–15 cycles as per qPCR results; 72°C for 2 min. Libraries were size-selected (0.5–0.2X dual-sided) with Ampure XP beads (Beckman Coulter, A63881) and sequenced to a depth of ~5 million reads (plasmid) or ~10 million reads (virus).

Sequencing data were analysed using the genBaRcode R package (v1.2.5), yielding a library diversity of approximately 0.25 million barcodes for both libraries, consistent with the original library diversity reported on Addgene.

Organoid infection

3 x 10^4 cells were aliquoted and incubated with 1.5 x 10^6 LARRY virus particles in 200 µL culture media lacking Cultrex under culture conditions (37°C, 5% CO_2, humidified atmosphere) for 1 hour. Cells were then split into 3 and plated in 12-well dishes pre-coated with a 150 µL layer of Cultrex RGF Basement Membrane Extract, type 2, PathClear®. After 3 days, media was removed and replaced with 1mL of indicated culture media and replaced in culture conditions. After 4 more days, approximately 30% of organoids were eGFP+ and were processed further.

Organoid enrichment using the VISIBLE system and tumour processing

The VISIBLE system comprises two independent units: a top unit, which features a robotic manipulation system with two interchangeable tool heads, and a bottom unit that is an automated fluorescence microscope. This system is described in detail elsewhere (CITATION) but briefly, the robotic manipulation consists of an XY gantry with tool-head and its motion is controlled by 2 stepper motors (Bipolar Hybrid Stepper Motor Nema 17) arranged in a core XY coordination. For motion control in Z axis, a customized in-house developed screw rail-based mechanism is employed with a stepper motor (Bipolar Hybrid Stepper Motor Nema 11). Mechanical limit switches are installed for homing the axes. Stepper motors and limit switches are controlled with firmware installed on Smothieboard V2. We have used open-source Pronterface software module for interactively controlling our robotic system. The bottom unit is a fluorescence inverted microscope procured from Zaber Technologies Inc with a 2.3-megapixel CMOS sensor (Hamamatsu ORCA-Spark C11440-36U). Images were acquired using a FITC filter (Semrock BrightLine full-multiband filter set, optimized for DAPI, FITC, & Texas Red) and the light source consists of 6 solid-state sources operating independently from Lumencor (SPECTRA X) with output spectral range between 360–780 nm. A 3 mm liquid light guide was used to connect the light source with the microscope chamber. Open-source micro-manager software was used to control and automate the microscope unit.

Using this system, eGFP+ organoids were picked, spun down, and resuspended in Matrigel (Corning Cat No. 354234) prior to injection into the 4th inguinal mammary gland. 5 weeks after injection of eGFP+ enriched organoids, tumours were collected, dissociated and human tumour cells were enriched using a Miltenyi tumour dissociator according to manufacturer's instructions. Briefly, tumour tissues were minced into 0.5-1.0 mm fragments with a sterile razor blade and this was transferred to a gentleMACS C tube (Order No. 130093-237). 4.7 mL DMEM was added along with enzymes A,R and H prior to running the 37C-h-

TDK3 program for 30 minutes. Samples were then incubated on ice for 5 minutes and 3-4 mL of supernatant was passed through a 70 µm strainer. The remaining tumour pieces were broken apart using the m-impTumor-01-01 program for 1 minute and this solution was passed through the same 70 µm strainer. The strainer was washed once with PBS and collected cells were pelleted by centrifuging at 1200 rpm for 5 minutes at 4°C, washed once with PB in 80 µL PBS+0.5% BSA. Cell suspension was incubated with 20 µL Miltenyi Mouse Cell Depletion cocktail antibody for 15 minutes at 4°C. Volume was adjusted to 500 µL and passed through a Miltenyi LS column (Order No. 130-042-401). Flow through containing enriched human tumour cells were collected and used subsequently for single cell RNA sequencing.

Organoid sorting

eGFP+ organoids were sorted by first treating with collagen and dispase followed by resuspending in 30 mL FACS buffer (1% BSA in PBS w/v) and sorting using a complex object parametric analyser and sorter (COPAS) VISION 250 particle sorter. The gating strategy used to identify LARRY expressing organoids was based on the optical density (Extinction 561 peak height), size (time of flight) and eGFP fluorescence (488 nm laser excitation and detected using a 512/26 bandpass filter). A neutral density ND 2.0 filter was used to prevent extinction signal saturation and the gating strategy was confirmed based on in-flow brightfield images. Sorted eGFP+ organoids were centrifuged and digested with accutase to obtain a single-cell suspension.

Single cell RNAsequencing

Single cell concentration and viability was measured using acridine orange (AO) and propidium iodide (PI) and the Luna-FX7 Automatic Cell Counter. Approximately 120 000 cells per tumour or 900-7300 cells per LEBTROSS sample were loaded on Chromium Chip and partitioned in nanolitre scale droplets using the Chromium Controller and Chromium Next GEM Single Cell Reagents (10x Genomics CG000315 Chromium Single Cell 3' Reagent Kits User Guide (v3.1 - Dual Index)). Within each droplet the cells were lysed, and the RNA was reverse transcribed. All of the resulting cDNA within a droplet shared the same cell barcode. Illumina compatible libraries were generated from the cDNA using Chromium Next GEM Single Cell library reagents in accordance with the manufacturer's instructions. Final libraries are QC'd using the Agilent TapeStation and sequenced using the Illumina NovaSeq 6000. Sequencing read configuration: 28-10-10-90.

Data processing and analysis

The GFP-LARRY plasmid was added to the reference genome refdata-gex-GRCh38-2020-A and the GTF annotation of the plasmid transcripts was added to the same reference annotation file. Cellranger (version 7.0.1) mkref was ran to create a new reference for genome an annotation. Cellranger count was used to count the 10x libraries.

The LARRY barcode information was obtained and extracted from the 10X GEX library and from the libraries containing the specifically amplified LARRY barcodes. To extract the unmapped reads and the reads that map to the LARRY-GFP plasmid (mRNA) from the 10X/CellRanger output, we identify those reads using samtools (version 1.15.1) (Li et al., 2009) and subsequently extract those reads from the 10X GEX fastq.gz files. The LARRY barcodes are extracted from the LARRY libraries by removing primer/adapter sequences with cutadapt (version 3.5) (Martin, 2011) followed a second round of cutadapt to extract the LARRY barcodes.

A whitelist of cell barcodes was obtained with UMI-tools (version 1.1.2) (T. Smith et al., 2017), specifically umi_tools extract, and after having ensured that each unique cell-barcode/UMI combination is associated with one LARRY barcode sequence, we grouped all the LARRY barcodes found within the same cell. For each cell barcode-LARRY barcode combination, we count the number of unique UMIs associated with each cell barcode-LARRY barcode combination. After having identified a set of Cell barcode-LARRY barcode - UMI counts for each of the samples, we next identify clonal groups for all samples.

The cellranger quantifications were imported into a Seurat (version 4.3.0) (Hao et al., 2021) object and doublets were calculated using scDblFinder (version 1.8.0) (Germain et al., 2022) and the LARRY barcode information was added to the Seurat objects. The R programming language was used (version 4.1.2)(R Development Core Team 2008). We investigated key QC parameters, and we remove cells with a low number of detected features or cells with a very high proportion of mitochondrial gene expression. We selected a lower bound filter for both the minimum number of reads per cell and the minimum number of detected features using 3 median absolute deviations (MADs). For the percentage of mitochondrial gene, we set upper bounds using 3 MADs.

Before investigating clonal groups across cluster (used as a proxy for cell state) we remove cells that are associated with more than one clonal group (i.e. LARRY barcode).

We use the "SCTransform" method (version 0.3.5) (Hafemeister & Satija, 2019) for the normalisation and variance stabilisation which, in comparison to the standard Seurat approach, sctransform returns 3000 variable features by default, instead of 2000.

Clonal groups are identified across all samples based on the combined library prep information for each sample. We investigate the percentage of cells in which LARRY barcodes were detected, the number of unique clonal groups, the number of detected clonal groups in cells with detected LARRY barcode, the number of cells within each clonal group.

Analysis of human breast cancer single cell RNA sequencing data

Gene modules were obtained from Wu et al., 2021, and human tumour data was downloaded from GEO GSE176078 and analysed using the Seurat package (version 4) (Hao et al., 2021).

Incucyte imaging and organoid growth analysis

Organoids were generated by plating 1 x 10^4 cells per well in a 48-well dish (Cat# 353078, FALCON) pre-coated with a 50 µL layer of Cultrex RGF Basement Membrane Extract, type 2, PathClear®. After 3 days, culture media was changed to culture media containing the indicated treatments. The plate was transferred to an Incucyte S3 live cell imaging instrument contained within a standard tissue culture incubator and allowed to equilibrate for 1-2 hours. Images were acquired with a 10X objective every 3 hours for 4 days to capture 33 time points. Within FIJI, images were made into stacks, stabilized and individual organoids were tracked using the TrackMate batcher plugin. Within this plugin, CellPose 2.0 was used to segment individual organoids and was used to identify tracks that lasted the entire length of the acquisition. Exponential growth curves were then fitted to each growth curve and a rate was determined for each organoid using custom Python code. Plots were then generated using the SuperPlotsOfData Shiny app or Graphpad (Goedhart, 2021).

Power calculation for modified Luria-Delbrück

The probability, or confidence, that none of the selected clones were resistors was given by:

$y = (1 - x)^n$

Where x is the probability of being a resistor and n is the number of clones selected. Solving for n, we found that from a population where 17% of cells are resistant, we would need to test at least 17 clonal populations to have a > 95% confidence that resistance is not a clonal feature.

Dual-view oblique plane microscopy imaging

Image acquisition

Organoids were generated by plating 1 x 10^4 cells per well in a ibidi 24 well µ-plate (Cat# 82426, ibidi) pre-coated with a 83 µL layer of Cultrex RGF Basement Membrane Extract, type 2, PathClear®. After 3 days, culture media was changed to phenol-red free imaging media. Imaging media consisted of SILAC Advanced DMEM/F-12 Flex, supplemented with 17.5 mM D-Glucose, 0.699 mM L-Arginine hydrochloride and 0.499 mM L-Lysine hydrochloride, along with additional supplements present in culture media. Organoids were imaged on a custom-built dual-view oblique plane microscopy (dOPM) system as previously described (Smith et al., 2023; Sparks et al., 2020; Sparks et al., in preparation). For each field of view, two dOPM views were acquired at ±35°, with z-planes spaced 1 µm apart and spanning a 150 µm depth (perpendicular to the imaging plane). Images were collected at 512 × 512 resolution with a pixel size of 0.35 µm in the sample space. The light-sheet width was approximately 3 µm FWHM at the waist. Two dOPM views were deskewed and fused using the Multiview Fusion plugin in FIJI (Preibisch et al., 2014), with affine registration derived from 3 µm UltraRainbow fluorescent beads (Spherotech, URFP-30-2) embedded in 2–4% agarose. Final volumes were converted to OME-TIFF format for further analysis. Two fused views were resliced and binned ×2 to produce isotropic 0.69 × 0.69 × 0.69 μm^3 voxels.

H2b, Akt activity and glucose biosensor were imaged using five fluorescence channels: eCFP (445 nm excitation, 483/32 nm emission), sensitized Citrine-FRET (445 nm/525/45 nm), direct Citrine (515 nm/542/20 nm), mRuby2 (561 nm/609/54 nm), and miRFP670nano (642 nm/697/58 nm). Each organoid was imaged immediately before treatment, 24, and 96 hours after drug treatment. The detection camera rolling shutter exposure time was set to 10 ms for all channels. All laser power levels were set to 100% within Omicron laser control software and NIS-elements acquisition software apart from 561 nm excitation which was set to 20% of maximum power. For each excitation wavelength, average power in the back focal plane was measured to be: 445 nm @ 2.4 mW, 515 nm @ 3.2 mW, 561 nm @ 0.8 mW and 642 nm @ 5.6 mW. All lasers were blanked so as to only be active during the camera exposure time.

Fixed organoids were processed according to the FLASH immunofluorescence protocol described for organoids (Messal et al., 2021). Briefly, organoids were fixed with a 4% paraformaldehyde solution, washed 3 times with PBS, FLASH reagent 2 was used for permeabilization, followed by washing with PBT, blocking, and overnight primary staining at 4 °C (1:1000, Krt14 Clone LL002 Cell Services Platform at the Francis Crick Institute). Organoids were washed with PBS, and stained with secondary (1:2000 Goat anti-rabbit 555 (Cat# A21428 Invitrogen)) for 1 hour at room temperature. Nuclei were counterstained with 0.5 µmL siR-DNA in PBST for 5 minutes at room temperature, followed by washing with PBS. Fluorescence imaging used 488 nm (Krt14, 525/45 nm) and 642 nm (nuclear, 697/58 nm) channels. Imaging used 20 ms exposure and 100% laser power for all channels.

Image processing

For each fluorescence channel, the background was removed using a threshold set at 1.4 times the background signal level determined from the mode of each image volume. For the glucose/AKT data, the nuclear channel was log-transformed.

Nuclear segmentation was performed using a nonlinear multiscale top-hat enhancement transform following Guglielmi et al., 2021 and Santos et al., 2008. This was performed by first smoothing with 3D Gaussian filters at three spatial scales of $\sigma_1 \approx 1.4$ µm, $\sigma_2 \approx 2.8$ µm, $\sigma_3 \approx 5.6$ µm (corresponding to kernel sizes of 2, 4, and 8 voxels at 0.7 µm/voxel), resulting in images U_1, U_2 and U_3 respectively. The enhancement used two paired scale comparisons: the normalized difference between U_1 and U_2, i.e. $(U_1-U_2)/U_2$, and between U_2 and U_3, i.e. $(U_2-U_3)/U_3$. These responses were combined linearly with a fixed mixing weight ($a_1 = 0.7$) to prioritize fine-scale structure. A global threshold was then applied to generate a binary mask. Threshold values were fixed per experiment (FUCCI, glucose/AKT, keratin) and tuned manually by inspecting representative volumes to optimize segmentation quality by eye.

Small holes were filled and thin structures removed using morphological operations. Objects smaller than ~3.5 µm in diameter (i.e. <125 voxels) were excluded. A 3D watershed refinement step was applied to separate touching nuclei, and objects at the volume border or outside the main organoid region were discarded.

In experiments with cytoplasmic biosensors (FRET, AKT, keratin), cytoplasmic “collar” regions were defined for each nucleus by performing two successive 1 µm 3D dilations of the nuclear mask. The collar was then extracted as the shell-like region between the second dilation and the original nucleus, excluding any areas overlapping nuclear or collar regions from neighbouring cells. Biosensor intensities were then quantified separately within nuclear and cytoplasmic compartments.

Feature Extraction

For each segmented nucleus and corresponding collar, summary statistics were computed for each fluorescence channel, including the mean, standard deviation, skewness, kurtosis, and 25th/50th/75th percentiles. FRET ratio (Citrine/CFP) was calculated as the ratio of corrected Citrine intensity to corrected CFP intensity. AKT activity was defined as:

AKT activity = median_cytoplasm(I_AKT) / [median_cytoplasm(I_AKT) + median_nucleus(I_AKT)]

where I_AKT refers to the background-corrected AKT intensity, and "median_cytoplasm" and "median_nucleus" denote the median intensity values within cytoplasmic collars and nuclei, respectively.

Voxel-wise biosensor overlays were generated by assigning per-object median values back into the segmented binary masks. These overlays were saved as five-channel OME-TIFF hyperstacks containing raw intensities, biosensor activity maps, and segmentation masks.

Proliferation Rate Estimation

To determine the proliferation rate of each organoid, the number of segmented nuclei per organoid was compared between timepoints. The per-organoid proliferation rate was calculated as:

Proliferation rate = (1 / Δt) × log(N_final / N_initial)

where Δt is the time interval in hours, N_initial is the number of nuclei at the starting time point, and N_final is the number at the later time point.

Bulk RNA sequencing

Organoids were generated by plating 3.5 x 10^4 cells per well of a 12-well plate. After 3 days, media was removed, cells lysed and mRNA isolated according to manufacturer's instructions, including on column Dnase digest (QIAGEN Rneasy mini kit).

Sequencing libraries were prepared using the KAPA mRNA HyperPrep Kit (Roche, kit code KK8581) according to manufacturer's instructions. Briefly, samples were normalised to 50 ng of RNA in a final volume of 50 µl. PolyA-tailed RNA was captured with 50 ul of capture beads at 65 °C for 2 min and 20 °C for 5 min. Beads were washed to remove other RNA species and RNA was eluted from the beads in 50 ul of RNase free water by incubating at 70 °C for 2 min and 20 °C for 5 min. A second capture of PolyA-tailed RNA was performed by adding 50 µl of bead binding buffer and the sample incubated for 5min at 20 °C. Beads were washed to remove other RNA species and eluted in 20 µl of Fragment, Prime and Elute Buffer. The fragmentation reaction was run for 6 min at 94 °C for a library insert size of 200-300 bp. Fragmented RNA underwent first and second strand cDNA synthesis according to manufacturer instructions. The KAPA Unique Dual-Indexed Adapters Kit (15µM) (Roche-KK8727) stock was diluted to 1.5 µM as recommended by the manufacturer for a total RNA input of 50 ng. The adaptor ligation was carried out by adding 5 µl of diluted adaptor and 45 µl of ligation mix (50 µl of ligation buffer + 10 µl of DNA ligase) to 60 µl of cDNA. The ligation reaction was run for 15 mins at 20 °C. To remove short fragments such as adapter dimers, two SPRISelect bead clean-ups were done (0.63x SPRI and 0.7x SPRI). To amplify the library, 25 µl of Kapa HiFi HotStart PCR master mix plus 5 µl of Library Amplification Primer mix was added to 20 µl cDNA and 14 PCR cycles were performed as recommended by the manufacturer for a total RNA input of 50 ng. Amplified libraries were purified via a SPRISelect 1x bead cleanup.

The quality and fragment size distributions of the purified libraries was assessed by a 4200 TapeStation Instrument (Agilent Technologies). An average of 25 million paired end reads per library (PE100) were generated on a NovaSeq6000 (Illumina). All samples were processed using the nf-core RNAseq pipeline (v.3.10.1) operating on Nextflow (v.22.10.3) (68, 69). Settings for individual tools were left as standard for this workflow version unless otherwise specified. Alignment to GRCm38 (release 95) was performed using STAR (v2.7.10a) (64), followed by quantification using RSEM (v1.3.1) (63). Results were further processed in R (version 4.2.0) (67). Outputs of the RNAseq pipeline were assessed for quality using the metrics provided by the pipeline's inbuilt quality control packages, PCA (package stats v4.2.0), and correlation analyses between samples (package stats v4.2.0). Differential expression analysis was performed with DESeq2 (v1.38.3) (66), using a model accounting for differences in replicate and treatment (~ replicate + treatment). The significance threshold for the identification of differentially expressed genes was set as an adjusted P value ≤0.05, where P values were adjusted for false discovery rates according to the Independent Hypothesis Weighting method (package IHW, v1.26.0) (70, 71). Bulk RNAseq data will be deposited in the Gene Expression Omnibus.

Metabolomics

Sample preparation

Organoids were generated by plating 150 000 cells per well into an ultra-low attachment 6-well plate (Corning ref. 3471) in organoid culture media described above. After 3 days of culture, organoids were collected, spun down (1300 rpm for 4 mins), rinsed with SILAC Advanced DMEM/F12 without glucose and resuspended in 2 mL Breast Cancer Organoid Media without glucose that was supplemented with 17.5 mM ^{13}C-Glucose, 91.25 mg/L L-lysine and 147.5 mg/L L-Arginine. Organoids were then replated on ultra-low attachment 6-well plates and incubated at 37°C and 5% CO_2. After 6 hours, organoids were collected, rinsed with 10 mL chilled PBS and put on ice. These were centrifuged for 3 minutes at 600 g in cooled

centrifuge and the supernatant along with as much of the matrigel layer as possible was aspirated without touching the cell pellet. 800 uL cold PBS was added and organoids were transferred to a chilled 2 mL Eppendorf tube. Samples were then centrifuged for 3 minutes at 600 g in a cooled centrifuge. Supernatant was pipetted off and 900uL MeOH containing 1 nmol scyllo-inositol was added. Samples were then frozen on dry ice and stored at -80°C. To extract metabolites, 300 uL $CHCl_3$ was added, followed by 300 uL H_20 to each sample. Samples were then vortexed briefly but vigorously and pulse sonicated in a sonicating water bath in a cold room (8 minutes ON, 7 minutes OFF for four cycles). Then, samples were centrifuged for 10 minutes at maximum speed (16 100g), supernatant transferred to a 2 mL eppendorf and stored at -80. The remaining cellular debris was used for DNA extraction using the PureLink Genomic DNA kit (ThermoFisher) and total DNA content quantified using a NanoDrop. Prior to GC-MS, metabolomic samples were dried in a speed vac. Each extract was partitioned using MeOH/Water/CHCl3 (150:150:50), vortexed briefly and centrifuged at 4°C for 10 min.

Gas Chromatography-Mass Spectrometry (GC-MS)

Data acquisition was performed using an Agilent 7890B-5977A GC-MSD in EI mode after derivatization of twice methanol-washed dried extracts by addition of 20 µL methoxyamine hydrochloride (20 mg/mL in pyridine (both Sigma), RT, >16 hrs) and 20 µL BSTFA + 1% TMCS (Sigma, RT, >1 hr). GC-MS parameters were as follows: carrier gas, helium; flow rate, 0.9 mL/min; column, DB-5MS+DG (30 m + 10 m × 0.25 mm, Agilent); inlet, 270°C; temperature gradient, 70°C (2 min), ramp to 295°C (12.5°C/min), ramp to 320°C (25°C/min, 3 min hold). Scan range was m/z 50-550. Data was acquired using MassHunter software (version B.07.02.1938). Data analysis was performed using MANIC software, an in house-developed adaptation of the GAVIN package (PMID: 21575589). Metabolites were identified and quantified by comparison to authentic standards, and label incorporation estimated as the percentage of the metabolite pool containing one or more ^{13}C atoms after correction for natural abundance.

Flow cytometry

Multiparametric flow cytometry was used for analysis of organoid cells. Organoids were dissociated and Cells were stained with a blue fixable Live/Dead dye (Invitrogen; Thermo Fisher Scientific) for the exclusion of dead cells before incubation with saturating concentrations of surface monoclonal antibodies (mAbs ADD details of the antibodies) diluted in 50% Brilliant violet buffer (BD Biosciences) and 50% PBS for 30 min at 4°C. Cells were fixed and permeabilised for further functional assessment with Cytofix/Cytoperm (BD Biosciences) according to the manufacturer's instructions. All samples were acquired in 1x PBS using a Cytek Aurora and analysed using FlowJo v10.10.0 (Tree Star). Doublets and dead cells were excluded from the analysis.

Multiplexed tumour imaging

Mammary tumours were generated by injecting tumour organoids under the nipple into the mammary fat pad. Vehicle or 130 mg/kg Capivasertib was administered twice daily by oral gavage for 4 days, followed by 3 days off. Upon reaching the experimental endpoint, mice were sacrificed and tumours collected for further processing. Fresh frozen sections were cut at 10µm and fixed for 20 minutes at 10% NBF. Slides were washed and incubated at 4°C for 10 minutes in solution of 2% H2O2 in methanol to block endogenous peroxidase. Slides were washed and then rinsed in 100% IMS and air dried before loading onto Leica Bond Rx platform. Antigen retrieval stripping steps between each antibody were performed with Epitope Retrieval Solution 1 (pH9) (Leica, AR9961) for 20 minutes at 95˚C. Slides were then incubated with 0.1% BSA-PBST solution for 5 minutes at RT for protein blocking prior to each antibody.

Multiplex immunofluorescence was performed on a BondRx Leica Bond Rx, and antibodies were applied with Opal pairings in the following order: Ki67 (abcam, ab15580) at 1:1500 dilution with Opal 570 (Akoya, FP1488001KT) at 1:300 dilution, Cytokeratin-14 (abcam, ab7800) at 1:500 dilution with Opal 520 (Akoya, FP1487001KT) at 1:300 dilution, pS6 (CST, 2211S) at 1:400 dilution with Opal 620 (Akoya, FP1495001KT) at 1:300 dilution, Laminin (Sigma, L9393) at 1:100 dilution with Opal 780 (Akoya, FP1501001KT) at 1:100 and 1:25 dilution. Anti-rabbit Polymer (Leica, RE7260-CE, RTU) was used as secondary for antibodies raised in rabbit and rabbit anti-mouse Post Primary (Leica, RE7260-CE, RTU) and anti-rabbit Polymer (Leica, RE7260-CE, RTU) were used as secondary for antibodies raised in mouse. Antibodies were diluted in 1xPlus automation amplification antibody diluent (Akoya, FP1609) except for pS6, which was diluted in 1X Antibody Diluent/Block (Akoya, ARD1001EA). Slides were counterstained with DAPI (Thermo Scientific, 62248) 1:2500 and mounted with Prolong Gold Antifade reagent (Invitrogen, P36934). Slides were scanned using the PhenoImager HT (formerly Vectra Polaris) using PhenoImager HT 2.0 software.

Figure legends

Figure 1. Non-genetic heterogeneity underpins response to Akt kinase inhibition. UMAP (uniform manifold approximation and projection) representation of GCRC1915 patient-derived xenograft single-cell RNA sequencing datasets with colours indicating **a**. cluster membership (resolution = 0.1) or **b**. LARRY barcode identity of the 5 largest clonal groups. **c**. Upset plot displaying cluster membership of clonal groups **d.** Plot of the results from a binomial test to evaluate the presence of clonal group members within more than one cluster. **e**. Growth rates of organoids treated with indicated drug conditions for 4 days. In the upper panel, data are represented as Superplots where dots represent organoids (n=8682), circles represent experimental means (n=3) and colours indicate experiment identity. In the lower panel, relative fractions of organoid growth rates for each condition is shown. **f**. Representative brightfield micrographs of GCRC1915 PDXOs. Scale, 50 µm. **g**. Schematic outline of organoids where colour represents clonal identity, followed by two possible experimental outcomes. **h.** Paired mean growth rates of GCRC1915 PDXO clones treated with DMSO or Capivasertib (n=3 or 5) with calculated p-values (Holm- Šídák's multiple comparison test).

Figure 2. Single-cell and whole organoid metrics of PI3K pathway activity quantified by OPM **a**. Schematic of organoids relative to the objective of the dual-view OPM. **b**. Schematic of the polycistronic construct encoding a nuclear marker, Akt activity reporter and intracellular glucose biosensor separated by P2A or T2A self-cleaving peptide sequences. **c**. Representative brightfield or fluorescent OPM micrographs of GCRC1915 PDXO organoids stably expressing the construct from **b**. Scale, 10 µm **d**. Representative masks of quantitative metrics derived from fluorescent construct. **e**. Digital montage of maximum project images of pseudo-coloured micrographs representing intracellular glucose levels (left) and Akt activity (right) from 50 DMSO (top) and 50 Capivasertib (bottom) treated organoids immediately prior to, 1 day or 4 days after treatment. Scale, 100 µm. **f, g. and h.** Principal component analysis of biosensor-derived metrics from **f.** single cells and **g.** median values of whole organoids (480 organoids, n=4 experimental replicates). Regions indicated in the bottom-right grey dashed box are shown above for individual treatments. **h.** Principal component analysis of biosensor-derived metrics from single cells of 7 organoids. Colours denote organoid identity.

Figure 3. Collective differences to Akt kinase inhibition underpin responses to Capivasertib. **a**. Heatmap representation of organoids. Each column represents an organoid and each row represents a cell from that organoid. Growth rates for organoids are plotted above and pseudo-colour represents single cell FRET or Akt activity. Organoids are arranged in order of increasing growth rate. Cells are arranged in order of increasing glucose FRET sensor signal. Insets encompass the bottom, middle and top 50 organoids in the dataset **b**. Heatmap representation of (top and middle) Spearman's correlation coefficients between OPM-derived metrics and (bottom) the difference between Capivasertib and DMSO-treated conditions. * $p < 0.05$ two-tailed **c**. Plotted proliferation rates of organoids with 1 µM Capivasertib as a function of the change in Akt values at day 1 relative to pretreatment values. **d**. Plotted change in Glucose values at day 4 relative to day 1 of organoids with 1 µM Capivasertib as a function of the change in Akt values at day 4 relative to day 1. **e**. Plotted proliferation rate from day 1 to day 4 of organoids with 1 µM Capivasertib as a function of the change in Akt values at day 4 relative to day 1.

Figure 4. Lineage tracing unveils inter-organoid differences in gene expression. **a**. UMAP representation of LARRY-barcoded GCRC1915 PDXO cells treated with DMSO or Capivasertib. **b**. Bar chart depicting the fraction of all cells made up by each cluster defined by gene expression. **c**. UMAP representation of LARRY-barcoded GCRC1915 PDXO cells with colours indicating gene expression levels **d.** Bar chart depicting the fraction of total cells in each cell cycle state split by treatment groups (DMSO or Capivasertib) and cluster. **e**. UMAP

representation of LARRY-barcoded GCRC1915 PDXO cells with colours indicating gene barcode identity of the 5 largest clonal groups. **f**. Upset plot displaying cluster membership of clonal groups. **g**. Histogram displaying the relative frequencies of the false discovery rates (FDR) for the presence of clonal group members within more than one cluster.

Figure 5. p63 confers resistance to Capivasertib **a**. Growth rates of organoids treated with DMSO or Capivasertib for 4 days. Data are represented as Superplots where dots represent organoids (n=570), circles represent experimental means (n=4) and colours indicate experiment identity. **b**. Volcano plot depicting differential gene expression of Capivasertib resistant organoids relative to DMSO controls. **c**. UMAP representation of LARRY-barcoded GCRC1915 PDXO cells with colours indicating upregulation of Capivasertib resistance gene signature defined by the top 200 upregulated genes identified in Capivasertib-resistant organoids. **d**. Venn diagram depicting the number and overlap of genes upregulated in Capivasertib-resistant organoids, as well as Clusters 2 and 3 depicted in Figure 4a. **e**. Barplots depicting gene set enrichment signature p-values for overlapping between datasets. **f**. Digital montage of maximum project images of pseudo-coloured micrographs representing DMSO Capivasertib-resistant and Capivasertib-rested organoid lines and associated quantification of normalised KRT14 staining intensity. Data are represented as Superplots where dots represent organoids (n=450), circles represent experimental means (n=3) and colours indicate experiment identity. **g**. Growth rates of organoids treated with DMSO or Capivasertib for 4 days. Data are represented as Superplots where dots represent organoids (n=1616), circles represent experimental means (n=3) and colours indicate experiment identity. * $p < 0.05$ **** $p < 0.0001$ (Holm- Šídák's multiple comparison test).

Figure 6. Capivasertib enriches for basal-like cells in TNBC tumours. **a and b.** UMAP representation of GCRC1915 patient-derived xenograft single-cell RNA sequencing datasets with colour representing **(a.)** upregulation of a gene signature defined by Capivasertib resistance and p63 target genes (CaRe63) and **(b.)** *KRT14* **c.** Barplots depicting gene set enrichment signature p-values from Cluster 3 marker genes. **d. & e.** Tumour growth curves of GCRC1915 PDXOX derived tumours (**c.** mean **d.** individual) treated with either vehicle or control (n=7 mice per group) ** $p < 0.05$. (Tukey's multiple comparison test) **f.** Multiplexed imaging micrographs of representative vehicle or Capivasertib-treated tumours. **g. & h.** Violin plots of cellular staining intensity in DMSO and Capivasertib-treated tumours for **g.** KRT14 and **h.** Ki67 **i.** UMAP representation of a human TNBC single-cell RNA sequencing dataset from Wu et al. with colour representing upregulation of a gene signature defined by Capivasertib resistance and p63 target genes (CaRe63) and (inset) patient identifier. **j.** Graphical model of cell state transitions and the impact of Akt inhibition on each of the cell states.

Supplemental Figure 1. Gene module expression in a PDXOX model of triple negative breast cancer. **a.** Schematic of experimental steps taken to prepare single-cell RNAseq datasets **b.** UMAP representation of GCRC1915 patient-derived xenograft single-cell RNA sequencing datasets with colours indicating expression of gene modules defined by Wu et al. **c.** Violin plots depicting the indicated gene module scores for cells within each cluster of the LARRY labelled PDXOX dataset. **** $p < 0.0001$ (Wilcoxon test).

Supplemental Figure 2. PDXO sensitivity to PI3K/Akt/mTOR pathway inhibitors. **a**. Growth rate of individual organoids treated with DMSO, 1 μM Capivasertib or 1 μM Ipatasertib are plotted as a function of their initial size. **b.** Representative brightfield micrographs of GCRC1915 PDXOs. Scale, 50 μm. **c.** Relative frequency histogram of organoid growth rates for each indicated condition. **d.** Growth rates of organoids treated with indicated drug

conditions for 4 days. Data are represented as Superplots where dots represent organoids (n=2263), circles represent experimental means (n=4) and colours indicate experiment identity. * $p < 0.05$ ***$p < 0.001$ **** $p < 0.0001$ (Holm- Šídák's multiple comparison test).

Supplemental Figure 3. Principal component analysis of biosensor-derived metrics from median values of whole organoids. Colour denotes treatment condition (DMSO – black & 1 μM Capivasertib red) and dot size indicates organoid growth rate between 0 and 96 hours.

Supplemental Figure 4. Overview of cellular and whole organoids metrics of PI3K pathway activity. **a**. Glucose levels and Akt activity levels of cells treated with indicated drug conditions. Data are represented as Superplots where dots represent cells (n=22 044), circles represent experimental means (n=4) and colours indicate experiment identity. **b**. Values of median glucose levels and Akt activity of organoids treated with indicated drug conditions. Data are represented as Superplots where dots represent median organoid levels (n=679), circles represent experimental means (n=4) and colours indicate experiment identity. **c.** Plotted proliferation rates of organoids with 1 μM Capivasertib against pretreatment glucose levels. **d.** Plotted proliferation rates of organoids with 1 μM Capivasertib against pretreatment organoid size. **e**. Plotted growth rates of organoids with DMSO or 1 μM Capivasertib against the change in FRET values from the glucose biosensor relative to the initial values. Spearman' correlation * $p < 0.05$ two-tailed

Supplemental Figure 5. Sorting whole fluorescent organoids. **a.** Representative images of organoids passing through the flow cell. **b.** Fluorescent micrograph and corresponding contour plot of parental or mEmerald expressing organoids sorted into a ultra-low adherent v-bottom well. **c.** Fluorescent micrographs of specific numbers of sorted mEmerald+ organoids. **d.** Values of organoid size derived from flow cell micrographs of sorted organoids treated with either DMSO or 1 μM Capivasertib. Data are represented as Superplots where dots represent organoids (n=490), circles represent experimental means (n=3) and colours indicate experiment identity. * $p < 0.05$ Unpaired two-tailed t-test.

Supplemental Figure 6. Metabolomic analysis of Capivasertib resistant organoids **a.** % 13-C-Glucose incorporation of selected glycolytic and TCA cycle intermediates in parental or Capivasertib resistant organoids treated with either DMSO or 1 μM Capivasertib. Data are represented as Superplots where dots represent technical replicates (8 or 9), circles represent biological replicate means (n=3) and colours indicate biological replicate identity. * $p < 0.05$ ** $p<0.01$ *** $p <0.001$

Supplemental Figure 7. Characterisation of Capivasertib-resistant and p63-overexpressing organoids **a.** Western blot from parental, resistant or rested GCRC1915 PDXOs treated with DMSO or 1 μM Capivasertib for 24 hours. **b.** Growth rates of parental or resistant organoids treated with indicated concentration of paclitaxel for 4 days. Data are represented as Superplots where dots represent organoids (n=1444), circles represent experimental means (n=3) and colours indicate experiment identity. **c.** Representative brightfield micrographs of GCRC1915 PDXOs. Scale, 50 μm. **d.** Superplot indicating the number of cells per organoid where dots represent organoids (n=449), circles represent biological replicate means (n=3) and colours indicate biological replicate identity. **e.** Scatter plot of relative KRT14 staining as a function of the cell count. Each point represents a single parental organoid (n=150). **f,g,h.** Barplot of flow cytometry analysis of organoid-derived cells stained for indicated markers. (n=3 or 4) **i.** Flow cytometry analysis of a α6 integrin low subpopulation in DMSO or Capivasertib-resistant organoids rested for the indicated periods. (n=3) **j.** Relative fractions of organoid growth rates derived from α6 integrin low, high or bulk-sorted cells. After 3 days of growth, organoids were imaged for 4 days. (n=3) **k.** Western blot of GCRC1915 PDXOs stably overexpressing the indicated constructs. **l, m, n.** Barplot of flow cytometry analysis of

organoid-derived cells stained for indicated markers. (n=3) ** $p<0.01$ *** $p<0.001$ **** $p<0.000$. (Dunnett's multiple comparison test)

References

Beghin, A., Grenci, G., Sahni, G., Guo, S., Rajendiran, H., Delaire, T., Mohamad Raffi, S. B., Blanc, D., de Mets, R., Ong, H. T., Galindo, X., Monet, A., Acharya, V., Racine, V., Levet, F., Galland, R., Sibarita, J.-B., & Viasnoff, V. (2022). Automated high-speed 3D imaging of organoid cultures with multi-scale phenotypic quantification. *Nature Methods*, *19*(7), 881–892. https://doi.org/10.1038/s41592-022-01508-0

Beumers, L., Vlachavas, E.-I., Borgoni, S., Schwarzmüller, L., Penso-Dolfin, L., Michels, B. E., Sofyali, E., Burmester, S., Heiss, D., Wilhelm, H., Yarden, Y., Helm, D., Will, R., Goncalves, A., & Wiemann, S. (2023). Clonal heterogeneity in ER+ breast cancer reveals the proteasome and PKC as potential therapeutic targets. *Npj Breast Cancer*, *9*(1), 97. https://doi.org/10.1038/s41523-023-00604-4

Bosch, A., Li, Z., Bergamaschi, A., Ellis, H., Toska, E., Prat, A., Tao, J. J., Spratt, D. E., Viola-Villegas, N. T., Castel, P., Minuesa, G., Morse, N., Rodón, J., Ibrahim, Y., Cortes, J., Perez-Garcia, J., Galvan, P., Grueso, J., Guzman, M., … Baselga, J. (2015). PI3K inhibition results in enhanced estrogen receptor function and dependence in hormone receptor-positive breast cancer. *Science Translational Medicine*. https://doi.org/10.1126/scitranslmed.aaa4442

Cheung, K. J., Gabrielson, E., Werb, Z., & Ewald, A. J. (2013). Collective Invasion in Breast Cancer Requires a Conserved Basal Epithelial Program. *Cell*, *155*(7), 1639–1651. https://doi.org/https://doi.org/10.1016/j.cell.2013.11.029

Conway, J. R. W., Warren, S. C., Herrmann, D., Murphy, K. J., Cazet, A. S., Vennin, C., Shearer, R. F., Killen, M. J., Magenau, A., Mélénec, P., Pinese, M., Nobis, M., Zaratzian, A., Boulghourjian, A., Da Silva, A. M., del Monte-Nieto, G., Adam, A. S. A., Harvey, R. P., Haigh, J. J., … Timpson, P. (2018). Intravital Imaging to Monitor Therapeutic Response in Moving Hypoxic Regions Resistant to PI3K Pathway Targeting in Pancreatic Cancer. *Cell Reports*, *23*(11), 3312–3326. https://doi.org/https://doi.org/10.1016/j.celrep.2018.05.038

de Medeiros, G., Ortiz, R., Strnad, P., Boni, A., Moos, F., Repina, N., Challet Meylan, L., Maurer, F., & Liberali, P. (2022). Multiscale light-sheet organoid imaging framework. *Nature Communications*, *13*(1), 4864. https://doi.org/10.1038/s41467-022-32465-z

Drost, J., & Clevers, H. (2018). Organoids in cancer research. *Nature Reviews Cancer*, *18*(7), 407–418. https://doi.org/10.1038/s41568-018-0007-6

Elkabets, M., Vora, S., Juric, D., Morse, N., Mino-Kenudson, M., Muranen, T., Tao, J., Campos, A. B., Rodon, J., Ibrahim, Y. H., Serra, V., Rodrik-Outmezguine, V., Hazra, S., Singh, S., Kim, P., Quadt, C., Liu, M., Huang, A., Rosen, N., … Baselga, J. (2013). MTORC1 inhibition is required for sensitivity to PI3K p110α inhibitors in PIK3CA-mutant breast cancer. *Science Translational Medicine*. https://doi.org/10.1126/scitranslmed.3005747

Ershov, D., Phan, M.-S., Pylvänäinen, J. W., Rigaud, S. U., Le Blanc, L., Charles-Orszag, A., Conway, J. R. W., Laine, R. F., Roy, N. H., Bonazzi, D., Duménil, G., Jacquemet, G., & Tinevez, J.-Y. (2022). TrackMate 7: integrating state-of-the-art segmentation algorithms into tracking pipelines. *Nature Methods*, *19*(7), 829–832. https://doi.org/10.1038/s41592-022-01507-1

Fabrice, A., Eva, C., Gabor, R., Mario, C., Sibylle, L., S, R. H., Hiroji, I., Pierfranco, C., A, M. I., Bella, K., Toshinari, Y., Yen-Shen, L., Kenichi, I., Masato, T., Zsuzsanna, P., Anne-

Sophie, L., David, M., Celine, W., Samit, H., & Dejan, J. (2019). Alpelisib for PIK3CA-Mutated, Hormone Receptor–Positive Advanced Breast Cancer. *New England Journal of Medicine*, *380*(20), 1929–1940. https://doi.org/10.1056/NEJMoa1813904

França, G. S., Baron, M., King, B. R., Bossowski, J. P., Bjornberg, A., Pour, M., Rao, A., Patel, A. S., Misirlioglu, S., Barkley, D., Tang, K. H., Dolgalev, I., Liberman, D. A., Avital, G., Kuperwaser, F., Chiodin, M., Levine, D. A., Papagiannakopoulos, T., Marusyk, A., … Yanai, I. (2024). Cellular adaptation to cancer therapy along a resistance continuum. *Nature*, *631*(8022), 876–883. https://doi.org/10.1038/s41586-024-07690-9

Fruman, D. A., Chiu, H., Hopkins, B. D., Bagrodia, S., Cantley, L. C., & Abraham, R. T. (2017). The PI3K Pathway in Human Disease. *Cell*, *170*(4), 605–635. https://doi.org/https://doi.org/10.1016/j.cell.2017.07.029

Germain, P. L., Robinson, M. D., Lun, A., Garcia Meixide, C., & Macnair, W. (2022). Doublet identification in single-cell sequencing data using scDblFinder. *F1000Research*, *10*. https://doi.org/10.12688/F1000RESEARCH.73600.2/DOI

Goedhart, J. (2021). SuperPlotsOfData - A web app for the transparent display and quantitative comparison of continuous data from different conditions. *Molecular Biology of the Cell*, *32*(6), 470–474. https://doi.org/10.1091/MBC.E20-09-0583/ASSET/IMAGES/LARGE/MBC-32-470-G003.JPEG

Goyal, Y., Busch, G. T., Pillai, M., Li, J., Boe, R. H., Grody, E. I., Chelvanambi, M., Dardani, I. P., Emert, B., Bodkin, N., Braun, J., Fingerman, D., Kaur, A., Jain, N., Ravindran, P. T., Mellis, I. A., Kiani, K., Alicea, G. M., Fane, M. E., … Raj, A. (2023). Diverse clonal fates emerge upon drug treatment of homogeneous cancer cells. *Nature*, *620*(7974), 651–659. https://doi.org/10.1038/s41586-023-06342-8

Grasset, E. M., Dunworth, M., Sharma, G., Loth, M., Tandurella, J., Cimino-Mathews, A., Gentz, M., Bracht, S., Haynes, M., Fertig, E. J., & Ewald, A. J. (2025). Triple-negative breast cancer metastasis involves complex epithelial-mesenchymal transition dynamics and requires vimentin. *Science Translational Medicine*, *14*(656), eabn7571. https://doi.org/10.1126/scitranslmed.abn7571

Gris-Oliver, A., Palafox, M., Monserrat, L., Brasó-Maristany, F., Òdena, A., Sánchez-Guixé, M., Ibrahim, Y. H., Villacampa, G., Grueso, J., Parés, M., Guzmán, M., Rodríguez, O., Bruna, A., Hirst, C. S., Barnicle, A., de Bruin, E. C., Reddy, A., Schiavon, G., Arribas, J., … Serra, V. (2020). Genetic Alterations in the PI3K/AKT Pathway and Baseline AKT Activity Define AKT Inhibitor Sensitivity in Breast Cancer Patient-derived Xenografts. *Clinical Cancer Research : An Official Journal of the American Association for Cancer Research*. https://doi.org/10.1158/1078-0432.CCR-19-3324

Gross, S. M., Dane, M. A., Bucher, E., & Heiser, L. M. (2019). Individual Cells Can Resolve Variations in Stimulus Intensity along the IGF-PI3K-AKT Signaling Axis. *Cell Systems*, *9*(6), 580-588.e4. https://doi.org/https://doi.org/10.1016/j.cels.2019.11.005

Guglielmi, L., Heliot, C., Kumar, S., Alexandrov, Y., Gori, I., Papaleonidopoulou, F., Barrington, C., East, P., Economou, A. D., French, P. M. W., McGinty, J., & Hill, C. S. (2021). Smad4 controls signaling robustness and morphogenesis by differentially contributing to the Nodal and BMP pathways. *Nature Communications*, *12*(1), 6374. https://doi.org/10.1038/s41467-021-26486-3

Guillen, K. P., Fujita, M., Butterfield, A. J., Scherer, S. D., Bailey, M. H., Chu, Z., DeRose, Y. S., Zhao, L., Cortes-Sanchez, E., Yang, C.-H., Toner, J., Wang, G., Qiao, Y., Huang, X., Greenland, J. A., Vahrenkamp, J. M., Lum, D. H., Factor, R. E., Nelson, E. W., … Welm, A. L. (2022). A human breast cancer-derived xenograft and organoid platform for drug discovery and precision oncology. *Nature Cancer*, *3*(2), 232–250. https://doi.org/10.1038/s43018-022-00337-6

Hafemeister, C., & Satija, R. (2019). Normalization and variance stabilization of single-cell RNA-seq data using regularized negative binomial regression. *Genome Biology*, *20*(1), 296. https://doi.org/10.1186/s13059-019-1874-1

Hao, Y., Hao, S., Andersen-Nissen, E., Mauck, W. M., Zheng, S., Butler, A., Lee, M. J., Wilk, A. J., Darby, C., Zager, M., Hoffman, P., Stoeckius, M., Papalexi, E., Mimitou, E. P., Jain, J., Srivastava, A., Stuart, T., Fleming, L. M., Yeung, B., … Satija, R. (2021). Integrated analysis of multimodal single-cell data. *Cell*, *184*(13), 3573-3587.e29. https://doi.org/https://doi.org/10.1016/j.cell.2021.04.048

Hirata, E., Girotti, M. R., Viros, A., Hooper, S., Spencer-Dene, B., Matsuda, M., Larkin, J., Marais, R., & Sahai, E. (2015). Intravital Imaging Reveals How BRAF Inhibition Generates Drug-Tolerant Microenvironments with High Integrin β1/FAK Signaling. *Cancer Cell*, *27*(4), 574–588. https://doi.org/https://doi.org/10.1016/j.ccell.2015.03.008

Joshi, S., Moreno-Gonzalez, C., Suklai, P., Carraro, E., Ratcliffe, C. D. H., Boezio, G. L. M., Konstantinou, G., Hagemann, C., Ameer-beg, S., Imbert, A., Sahai, E., Tedesco, F. S., & Serio, A. (2025). VISIBLE: An imaging-driven system for sampling, biofabrication, and manipulation of complex biological models. *BioRXiv*.

Juric, D., Castel, P., Griffith, M., Griffith, O. L., Won, H. H., Ellis, H., Ebbesen, S. H., Ainscough, B. J., Ramu, A., Iyer, G., Shah, R. H., Huynh, T., Mino-Kenudson, M., Sgroi, D., Isakoff, S., Thabet, A., Elamine, L., Solit, D. B., Lowe, S. W., … Scaltriti, M. (2015). Convergent loss of PTEN leads to clinical resistance to a PI(3)Kα inhibitor. *Nature*. https://doi.org/10.1038/nature13948

Juric, D., Krop, I., Ramanathan, R. K., Wilson, T. R., Ware, J. A., Sanabria Bohorquez, S. M., Savage, H. M., Sampath, D., Salphati, L., Lin, R. S., Jin, H., Parmar, H., Hsu, J. Y., Von Hoff, D. D., & Baselga, J. (2017). Phase I Dose-Escalation Study of Taselisib, an Oral PI3K Inhibitor, in Patients with Advanced Solid Tumors. *Cancer Discovery*, *7*(7), 704–715. https://doi.org/10.1158/2159-8290.CD-16-1080

Juric, D., Rodon, J., Tabernero, J., Janku, F., Burris, H. A., Schellens, J. H. M., Middleton, M. R., Berlin, J., Schuler, M., Marta, G. M., Rugo, H. S., Ruth, S. B., Huang, A., Bootle, D., Demanse, D., Blumenstein, L., Coughlin, C., Quadt, C., & Baselga, J. (2018). Phosphatidylinositol 3-kinase a–selective inhibition with alpelisib (BYL719) in PIK3CA-altered solid tumors: Results from the first-in-human study. *Journal of Clinical Oncology*. https://doi.org/10.1200/JCO.2017.72.7107

Keenan, A. B., Torre, D., Lachmann, A., Leong, A. K., Wojciechowicz, M. L., Utti, V., Jagodnik, K. M., Kropiwnicki, E., Wang, Z., & Ma'ayan, A. (2019). ChEA3: transcription factor enrichment analysis by orthogonal omics integration. *Nucleic Acids Research*, *47*(W1), W212–W224. https://doi.org/10.1093/nar/gkz446

Khalil, A. A., Smits, D., Haughton, P. D., Koorman, T., Jansen, K. A., Verhagen, M. P., van der Net, M., van Zwieten, K., Enserink, L., Jansen, L., El-Gammal, A. G., Visser, D., Pasolli, M., Tak, M., Westland, D., van Diest, P. J., Moelans, C. B., Roukens, M. G.,

Tavares, S., … de Rooij, J. (2024). A YAP-centered mechanotransduction loop drives collective breast cancer cell invasion. *Nature Communications*, *15*(1), 4866. https://doi.org/10.1038/s41467-024-49230-z

Koboldt, D. C., Fulton, R. S., McLellan, M. D., Schmidt, H., Kalicki-Veizer, J., McMichael, J. F., Fulton, L. L., Dooling, D. J., Ding, L., Mardis, E. R., Wilson, R. K., Ally, A., Balasundaram, M., Butterfield, Y. S. N., Carlsen, R., Carter, C., Chu, A., Chuah, E., Chun, H. J. E., … Palchik, J. D. (2012). Comprehensive molecular portraits of human breast tumours. *Nature*. https://doi.org/10.1038/nature11412

Kondo, H., Ratcliffe, C. D. H., Hooper, S., Ellis, J., MacRae, J. I., Hennequart, M., Dunsby, C. W., Anderson, K. I., & Sahai, E. (2021). Single-cell resolved imaging reveals intra-tumor heterogeneity in glycolysis, transitions between metabolic states, and their regulatory mechanisms. *Cell Reports*, *34*(7), 108750. https://doi.org/https://doi.org/10.1016/j.celrep.2021.108750

Krieger, T. G., Le Blanc, S., Jabs, J., Ten, F. W., Ishaque, N., Jechow, K., Debnath, O., Leonhardt, C.-S., Giri, A., Eils, R., Strobel, O., & Conrad, C. (2021). Single-cell analysis of patient-derived PDAC organoids reveals cell state heterogeneity and a conserved developmental hierarchy. *Nature Communications*, *12*(1), 5826. https://doi.org/10.1038/s41467-021-26059-4

Le Marois, A., Bailey, S., Hooper, S., Kumar, S., Sparks, H., Alexandrov, Y., Caswell, D., Fröhlich, F., Schlegelmilch, K., Valand, K., Martin, M., Narvaez, A., Swanton, C., Downward, J., Dunsby, C., French, P., & Sahai, E. (2024). Imaging of MAP kinase dynamics reveals endocytic regulation of pulsatile signalling and network re-wiring in response to targeted therapy in EGFR-mutant non-small cell lung cancer. *BioRxiv*, 2024.05.14.594112. https://doi.org/10.1101/2024.05.14.594112

Le, X., Antony, R., Razavi, P., Treacy, D. J., Luo, F., Ghandi, M., Castel, P., Scaltriti, M., Baselga, J., & Garraway, L. A. (2016). Systematic functional characterization of resistance to PI3K inhibition in breast cancer. *Cancer Discovery*. https://doi.org/10.1158/2159-8290.CD-16-0305

Leroy, C., Ramos, P., Cornille, K., Bonenfant, D., Fritsch, C., Voshol, H., & Bentires-Alj, M. (2016). Activation of IGF1R/p110β/AKT/mTOR confers resistance to α-specific PI3K inhibition. *Breast Cancer Research*. https://doi.org/10.1186/s13058-016-0697-1

LeSavage, B. L., Suhar, R. A., Broguiere, N., Lutolf, M. P., & Heilshorn, S. C. (2022). Next-generation cancer organoids. *Nature Materials*, *21*(2), 143–159. https://doi.org/10.1038/s41563-021-01057-5

Li, H., Handsaker, B., Wysoker, A., Fennell, T., Ruan, J., Homer, N., Marth, G., Abecasis, G., & Durbin, R. (2009). The Sequence Alignment/Map format and SAMtools. *Bioinformatics*, *25*(16), 2078. https://doi.org/10.1093/BIOINFORMATICS/BTP352

Madsen, R. R., Vanhaesebroeck, B., & Semple, R. K. (2018). Cancer-Associated PIK3CA Mutations in Overgrowth Disorders. *Trends Mol Med*, *24*(10), 856–870. https://doi.org/10.1016/j.molmed.2018.08.003

Mahendralingam, M. J., Kim, H., McCloskey, C. W., Aliar, K., Casey, A. E., Tharmapalan, P., Pellacani, D., Ignatchenko, V., Garcia-Valero, M., Palomero, L., Sinha, A., Cruickshank, J., Shetty, R., Vellanki, R. N., Koritzinsky, M., Stambolic, V., Alam, M., Schimmer, A. D., Berman, H. K., … Khokha, R. (2021). Mammary epithelial cells have lineage-rooted

metabolic identities. *Nature Metabolism*, *3*(5), 665–681. https://doi.org/10.1038/s42255-021-00388-6

Maioli, V., Chennell, G., Sparks, H., Lana, T., Kumar, S., Carling, D., Sardini, A., & Dunsby, C. (2016). Time-lapse 3-D measurements of a glucose biosensor in multicellular spheroids by light sheet fluorescence microscopy in commercial 96-well plates. *Scientific Reports*, *6*(1), 37777. https://doi.org/10.1038/srep37777

Marsolier, J., Prompsy, P., Durand, A., Lyne, A.-M., Landragin, C., Trouchet, A., Bento, S. T., Eisele, A., Foulon, S., Baudre, L., Grosselin, K., Bohec, M., Baulande, S., Dahmani, A., Sourd, L., Letouzé, E., Salomon, A.-V., Marangoni, E., Perié, L., & Vallot, C. (2022). H3K27me3 conditions chemotolerance in triple-negative breast cancer. *Nature Genetics*, *54*(4), 459–468. https://doi.org/10.1038/s41588-022-01047-6

Martin, M. (2011). Cutadapt removes adapter sequences from high-throughput sequencing reads. *EMBnet.Journal*, *17*(1), 10–12. https://doi.org/10.14806/EJ.17.1.200

Mayer, I. A., Abramson, V. G., Isakoff, S. J., Forero, A., Balko, J. M., Kuba, M. G., Sanders, M. E., Yap, J. T., Van den Abbeele, A. D., Li, Y., Cantley, L. C., Winer, E., & Arteaga, C. L. (2014). Stand Up to Cancer Phase Ib Study of Pan-Phosphoinositide-3-Kinase Inhibitor Buparlisib With Letrozole in Estrogen Receptor-Positive/Human Epidermal Growth Factor Receptor 2-Negative Metastatic Breast Cancer. *Journal of Clinical Oncology*, *32*(12), 1202–1209. https://doi.org/10.1200/JCO.2013.54.0518

Messal, H. A., Almagro, J., Zaw Thin, M., Tedeschi, A., Ciccarelli, A., Blackie, L., Anderson, K. I., Miguel-Aliaga, I., van Rheenen, J., & Behrens, A. (2021). Antigen retrieval and clearing for whole-organ immunofluorescence by FLASH. *Nature Protocols*, *16*(1), 239–262. https://doi.org/10.1038/s41596-020-00414-z

Nguyen, N. T. B., Gevers, S., Kok, R. N. U., Burgering, L. M., Neikes, H., Akkerman, N., Betjes, M. A., Ludikhuize, M. C., Gulersonmez, C., Stigter, E. C. A., Vercoulen, Y., Drost, J., Clevers, H., Vermeulen, M., van Zon, J. S., Tans, S. J., Burgering, B. M. T., & Rodríguez Colman, M. J. (2025). Lactate controls cancer stemness and plasticity through epigenetic regulation. *Cell Metabolism*, *37*(4), 903-919.e10. https://doi.org/https://doi.org/10.1016/j.cmet.2025.01.002

Oliinyk, O. S., Shemetov, A. A., Pletnev, S., Shcherbakova, D. M., & Verkhusha, V. V. (2019). Smallest near-infrared fluorescent protein evolved from cyanobacteriochrome as versatile tag for spectral multiplexing. *Nature Communications*. https://doi.org/10.1038/s41467-018-08050-8

Oren, Y., Tsabar, M., Cuoco, M. S., Amir-Zilberstein, L., Cabanos, H. F., Hütter, J.-C., Hu, B., Thakore, P. I., Tabaka, M., Fulco, C. P., Colgan, W., Cuevas, B. M., Hurvitz, S. A., Slamon, D. J., Deik, A., Pierce, K. A., Clish, C., Hata, A. N., Zaganjor, E., … Regev, A. (2021). Cycling cancer persister cells arise from lineages with distinct programs. *Nature*, *596*(7873), 576–582. https://doi.org/10.1038/s41586-021-03796-6

Pachitariu, M., & Stringer, C. (2022). Cellpose 2.0: how to train your own model. *Nature Methods*, *19*(12), 1634–1641. https://doi.org/10.1038/s41592-022-01663-4

Ponsioen, B., Post, J. B., Buissant des Amorie, J. R., Laskaris, D., van Ineveld, R. L., Kersten, S., Bertotti, A., Sassi, F., Sipieter, F., Cappe, B., Mertens, S., Verlaan-Klink, I., Boj, S. F., Vries, R. G. J., Rehmann, H., Vandenabeele, P., Riquet, F. B., Trusolino, L., Bos, J. L., & Snippert, H. J. G. (2021). Quantifying single-cell ERK dynamics in colorectal cancer organoids reveals EGFR as an amplifier of oncogenic MAPK pathway

signalling. *Nature Cell Biology*, *23*(4), 377–390. https://doi.org/10.1038/s41556-021-00654-5

Preibisch, S., Amat, F., Stamataki, E., Sarov, M., Singer, R. H., Myers, E., & Tomancak, P. (2014). Efficient Bayesian-based multiview deconvolution. *Nature Methods*, *11*(6), 645–648. https://doi.org/10.1038/nmeth.2929

Roerink, S. F., Sasaki, N., Lee-Six, H., Young, M. D., Alexandrov, L. B., Behjati, S., Mitchell, T. J., Grossmann, S., Lightfoot, H., Egan, D. A., Pronk, A., Smakman, N., van Gorp, J., Anderson, E., Gamble, S. J., Alder, C., van de Wetering, M., Campbell, P. J., Stratton, M. R., & Clevers, H. (2018). Intra-tumour diversification in colorectal cancer at the single-cell level. *Nature*, *556*(7702), 457–462. https://doi.org/10.1038/s41586-018-0024-3

Russo, M., Crisafulli, G., Sogari, A., Reilly, N. M., Arena, S., Lamba, S., Bartolini, A., Amodio, V., Magrì, A., Novara, L., Sarotto, I., Nagel, Z. D., Piett, C. G., Amatu, A., Sartore-Bianchi, A., Siena, S., Bertotti, A., Trusolino, L., Corigliano, M., … Bardelli, A. (2019). Adaptive mutability of colorectal cancers in response to targeted therapies. *Science*, *366*(6472), 1473–1480. https://doi.org/10.1126/science.aav4474

Sanchez-Vega, F., Mina, M., Armenia, J., Chatila, W. K., Luna, A., La, K. C., Dimitriadoy, S., Liu, D. L., Kantheti, H. S., Saghafinia, S., Chakravarty, D., Daian, F., Gao, Q., Bailey, M. H., Liang, W.-W., Foltz, S. M., Shmulevich, I., Ding, L., Heins, Z., … Schultz, N. (2018). Oncogenic Signaling Pathways in The Cancer Genome Atlas. *Cell*, *173*(2), 321-337.e10. https://doi.org/https://doi.org/10.1016/j.cell.2018.03.035

Santos, A. F., Zaltsman, A. B., Martin, R. C., Kuzmin, A., Alexandrov, Y., Roquemore, E. P., Jessop, R. A., Erck, M. G. M. van, & Verheijen, J. H. (2008). Angiogenesis: An Improved In Vitro Biological System and Automated Image-Based Workflow to Aid Identification and Characterization of Angiogenesis and Angiogenic Modulators. *ASSAY and Drug Development Technologies*, *6*(5), 693–710. https://doi.org/10.1089/adt.2008.146

Savage, P., Pacis, A., Kuasne, H., Liu, L., Lai, D., Wan, A., Dankner, M., Martinez, C., Muñoz-Ramos, V., Pilon, V., Monast, A., Zhao, H., Souleimanova, M., Annis, M. G., Aguilar-Mahecha, A., Lafleur, J., Bertos, N. R., Asselah, J., Bouganim, N., … Park, M. (2020). Chemogenomic profiling of breast cancer patient-derived xenografts reveals targetable vulnerabilities for difficult-to-treat tumors. *Communications Biology*, *3*(1), 310. https://doi.org/10.1038/s42003-020-1042-x

Schade, A. E., Perurena, N., Yang, Y., Rodriguez, C. L., Krishnan, A., Gardner, A., Loi, P., Xu, Y., Nguyen, V. T. M., Mastellone, G. M., Pilla, N. F., Watanabe, M., Ota, K., Davis, R. A., Mattioli, K., Xiang, D., Zoeller, J. J., Lin, J.-R., Morganti, S., … Cichowski, K. (2024). AKT and EZH2 inhibitors kill TNBCs by hijacking mechanisms of involution. *Nature*, *635*(8039), 755–763. https://doi.org/10.1038/s41586-024-08031-6

Schmid, P., Abraham, J., Chan, S., Wheatley, D., Brunt, M., Nemsadze, G., Baird, R., Park, Y. H., Hall, P., Perren, T., Stein, R. C., László, M., Ferrero, J.-M., Phillips, M., Conibear, J., Sarker, S.-J., Prendergast, A., Cartwright, H., Mousa, K., & Turner, N. C. (2018). AZD5363 plus paclitaxel versus placebo plus paclitaxel as first-line therapy for metastatic triple-negative breast cancer (PAKT): A randomised, double-blind, placebo-controlled, phase II trial. *Journal of Clinical Oncology*. https://doi.org/10.1200/jco.2018.36.15_suppl.1007

Schmid, P., Cortes, J., Robson, M. E., Iwata, H., Hegg, R., Nechaeva, M., Xu, B., Verma, S., Haddad, V., Rodrigo Imedio, E., Schiavon, G., Foxley, A., & Park, Y. H. (2020). A phase III trial of capivasertib and paclitaxel in first-line treatment of patients with metastatic triple-negative breast cancer (CAPItello290). *Journal of Clinical Oncology*. https://doi.org/10.1200/jco.2020.38.15_suppl.tps1109

Sharma, S. V, Lee, D. Y., Li, B., Quinlan, M. P., Takahashi, F., Maheswaran, S., McDermott, U., Azizian, N., Zou, L., Fischbach, M. A., Wong, K.-K., Brandstetter, K., Wittner, B., Ramaswamy, S., Classon, M., & Settleman, J. (2010). A Chromatin-Mediated Reversible Drug-Tolerant State in Cancer Cell Subpopulations. *Cell*, *141*(1), 69–80. https://doi.org/https://doi.org/10.1016/j.cell.2010.02.027

Simond, A. M., Rao, T., Zuo, D., Zhao, J. J., & Muller, W. J. (2017). ErbB2-positive mammary tumors can escape PI3K-p110α loss through downregulation of the Pten tumor suppressor. *Oncogene*. https://doi.org/10.1038/onc.2017.264

Smith, M. B., Sparks, H., Almagro, J., Chaigne, A., Behrens, A., Dunsby, C., & Salbreux, G. (2023). Active mesh and neural network pipeline for cell aggregate segmentation. *Biophysical Journal*, *122*(9), 1586–1599. https://doi.org/https://doi.org/10.1016/j.bpj.2023.03.038

Smith, T., Heger, A., & Sudbery, I. (2017). UMI-tools: Modeling sequencing errors in Unique Molecular Identifiers to improve quantification accuracy. *Genome Research*, *27*(3), 491–499. https://doi.org/10.1101/GR.209601.116/-/DC1

Sparks, H., Dent, L., Bakal, C., Behrens, A., Salbreux, G., & Dunsby, C. (2020). Dual-view oblique plane microscopy (dOPM). *Biomed. Opt. Express*, *11*(12), 7204–7220. https://doi.org/10.1364/BOE.409781

Sparks, H., Kondo, H., Hooper, S., Munro, I., Kennedy, G., Dunsby, C., French, P., & Sahai, E. (2018). Heterogeneity in tumor chromatin-doxorubicin binding revealed by in vivo fluorescence lifetime imaging confocal endomicroscopy. *Nature Communications*. https://doi.org/10.1038/s41467-018-04820-6

Takanaga, H., Chaudhuri, B., & Frommer, W. B. (2008). GLUT1 and GLUT9 as major contributors to glucose influx in HepG2 cells identified by a high sensitivity intramolecular FRET glucose sensor. *Biochimica et Biophysica Acta (BBA) - Biomembranes*, *1778*(4), 1091–1099. https://doi.org/https://doi.org/10.1016/j.bbamem.2007.11.015

Turner, N. C., Alarcón, E., Armstrong, A. C., Philco, M., López Chuken, Y. A., Sablin, M.-P., Tamura, K., Gómez Villanueva, A., Pérez-Fidalgo, J. A., Cheung, S. Y. A., Corcoran, C., Cullberg, M., Davies, B. R., de Bruin, E. C., Foxley, A., Lindemann, J. P. O., Maudsley, R., Moschetta, M., Outhwaite, E., … Oliveira, M. (2019). BEECH: a dose-finding run-in followed by a randomised phase II study assessing the efficacy of AKT inhibitor capivasertib (AZD5363) combined with paclitaxel in patients with estrogen receptor-positive advanced or metastatic breast cancer, and in a PIK3CA mutant sub-population. *Annals of Oncology*, *30*(5), 774–780. https://doi.org/https://doi.org/10.1093/annonc/mdz086

Turner, N. C., Oliveira, M., Howell, S. J., Dalenc, F., Cortes, J., Moreno, H. L. G., Hu, X., Jhaveri, K., Krivorotko, P., Loibl, S., Murillo, S. M., Okera, M., Park, Y. H., Sohn, J., Toi, M., Tokunaga, E., Yousef, S., Zhukova, L., de Bruin, E. C., … Rugo, H. S. (2023).

Capivasertib in Hormone Receptor–Positive Advanced Breast Cancer. *New England Journal of Medicine*, *388*(22), 2058–2070. https://doi.org/10.1056/NEJMoa2214131

Varkaris, A., Fece de la Cruz, F., Martin, E. E., Norden, B. L., Chevalier, N., Kehlmann, A. M., Leshchiner, I., Barnes, H., Ehnstrom, S., Stavridi, A. M., Yuan, X., Kim, J. S., Ellis, H., Papatheodoridi, A., Gunaydin, H., Danysh, B. P., Parida, L., Sanidas, I., Ji, Y., … Juric, D. (2024). Allosteric PI3Kα Inhibition Overcomes On-target Resistance to Orthosteric Inhibitors Mediated by Secondary PIK3CA Mutations. *Cancer Discovery*, *14*(2), 227–239. https://doi.org/10.1158/2159-8290.CD-23-0704/729919/AM/ALLOSTERIC-PI3K-ALPHA-INHIBITION-OVERCOMES-ON

Varkaris, A., Pazolli, E., Gunaydin, H., Wang, Q., Pierce, L., Boezio, A. A., Bulku, A., DiPietro, L., Fridrich, C., Frost, A., Giordanetto, F., Hamilton, E. P., Harris, K., Holliday, M., Hunter, T. L., Iskandar, A., Ji, Y., Larivée, A., LaRochelle, J. R., … Kipp, D. R. (2024). Discovery and Clinical Proof-of-Concept of RLY-2608, a First-in-Class Mutant-Selective Allosteric PI3Kα Inhibitor That Decouples Antitumor Activity from Hyperinsulinemia. *Cancer Discovery*, *14*(2), 240–257. https://doi.org/10.1158/2159-8290.CD-23-0944/729922/AM/DISCOVERY-AND-CLINICAL-PROOF-OF-CONCEPT-OF-RLY

Vasan, N., Razavi, P., Johnson, J. L., Shao, H., Shah, H., Antoine, A., Ladewig, E., Gorelick, A., Lin, T.-Y., Toska, E., Xu, G., Kazmi, A., Chang, M. T., Taylor, B. S., Dickler, M. N., Jhaveri, K., Chandarlapaty, S., Rabadan, R., Reznik, E., … Baselga, J. (2019). Double PIK3CA mutations in cis increase oncogenicity and sensitivity to PI3Kα inhibitors. *Science*, *366*(6466), 714 LP – 723. https://doi.org/10.1126/science.aaw9032

Weinreb, C., Rodriguez-Fraticelli, A., Camargo, F. D., & Klein, A. M. (2020). Lineage tracing on transcriptional landscapes links state to fate during differentiation. *Science*, *367*(6479), eaaw3381. https://doi.org/10.1126/science.aaw3381

Wu, S. Z., Al-Eryani, G., Roden, D. L., Junankar, S., Harvey, K., Andersson, A., Thennavan, A., Wang, C., Torpy, J. R., Bartonicek, N., Wang, T., Larsson, L., Kaczorowski, D., Weisenfeld, N. I., Uytingco, C. R., Chew, J. G., Bent, Z. W., Chan, C.-L., Gnanasambandapillai, V., … Swarbrick, A. (2021). A single-cell and spatially resolved atlas of human breast cancers. *Nature Genetics*, *53*(9), 1334–1347. https://doi.org/10.1038/s41588-021-00911-1

Wuidart, A., Sifrim, A., Fioramonti, M., Matsumura, S., Brisebarre, A., Brown, D., Centonze, A., Dannau, A., Dubois, C., Van Keymeulen, A., Voet, T., & Blanpain, C. (2018). Early lineage segregation of multipotent embryonic mammary gland progenitors. *Nature Cell Biology*, *20*(6), 666–676. https://doi.org/10.1038/s41556-018-0095-2

Figure 1.

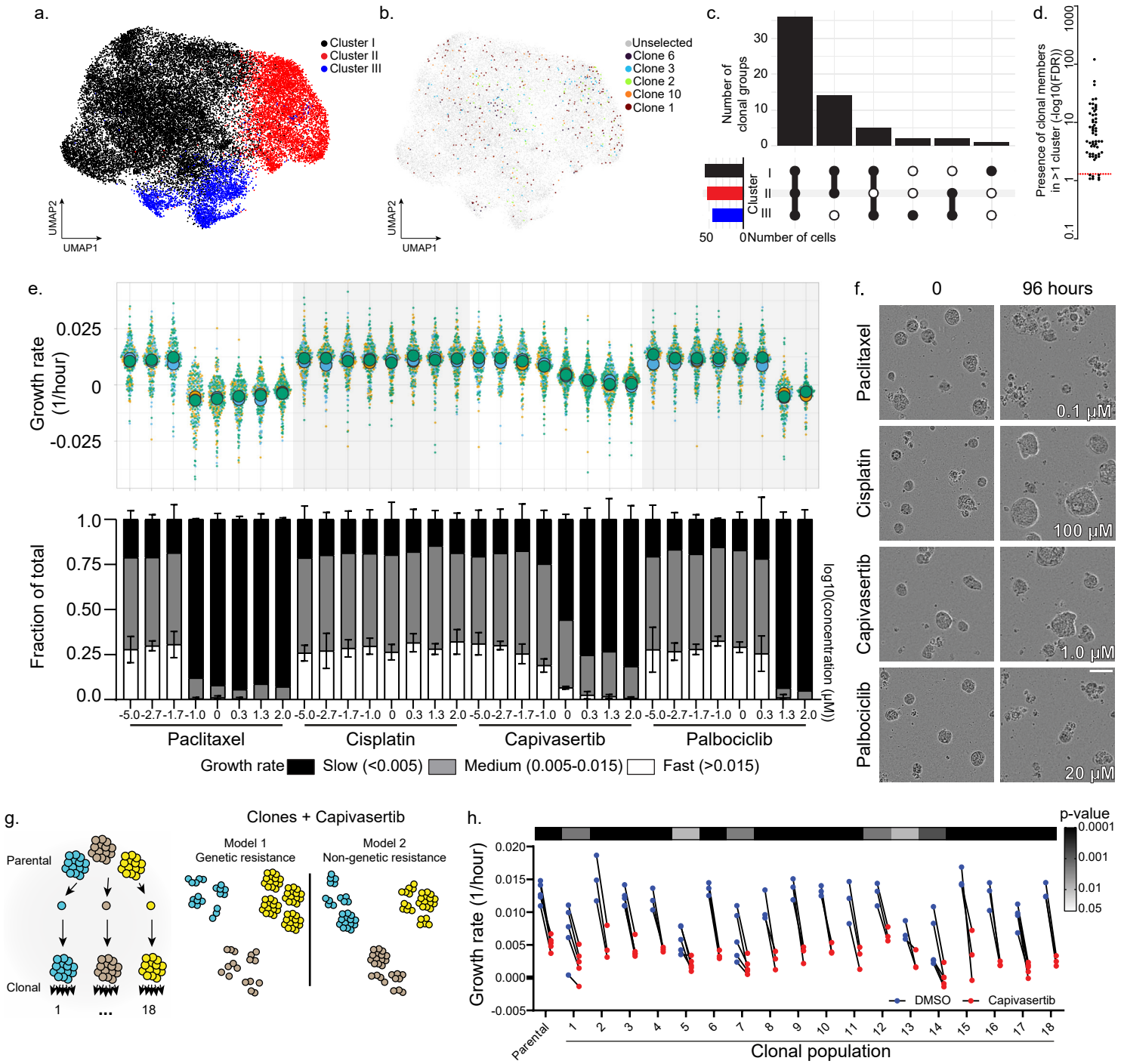
a.
Cluster I
Cluster II
Cluster III
UMAP2
UMAP1
b.
Unselected
Clone 6
Clone 3
Clone 2
Clone 10
Clone 1
UMAP2
UMAP1
c.
Number of clonal groups
30
20
10
0
Cluster
I
II
III
50
0
Number of cells
d.
Presence of clonal members in >1 cluster (-log10(FDR))
1000
100
10
1
0.1
e.
Growth rate (1/hour)
0.025
0
-0.025
Fraction of total
1.0
0.75
0.50
0.25
0.0
-5.0 -2.7 -1.7 -1.0 0 0.3 1.3 2.0
log10(concentration (μM))
Paclitaxel
Cisplatin
Capivasertib
Palbociclib
Growth rate
Slow (<0.005)
Medium (0.005-0.015)
Fast (>0.015)
f.
0
96 hours
Paclitaxel
0.1 μM
Cisplatin
100 μM
Capivasertib
1.0 μM
Palbociclib
20 μM
g.
Parental
Clonal
1
...
18
Clones + Capivasertib
Model 1
Genetic resistance
Model 2
Non-genetic resistance
h.
p-value
0.0001
0.001
0.01
0.05
Growth rate (1/hour)
0.020
0.015
0.010
0.005
0.000
-0.005
DMSO
Capivasertib
Parental
1 2 3 4 5 6 7 8 9 10 11 12 13 14 15 16 17 18
Clonal population

Figure 2.

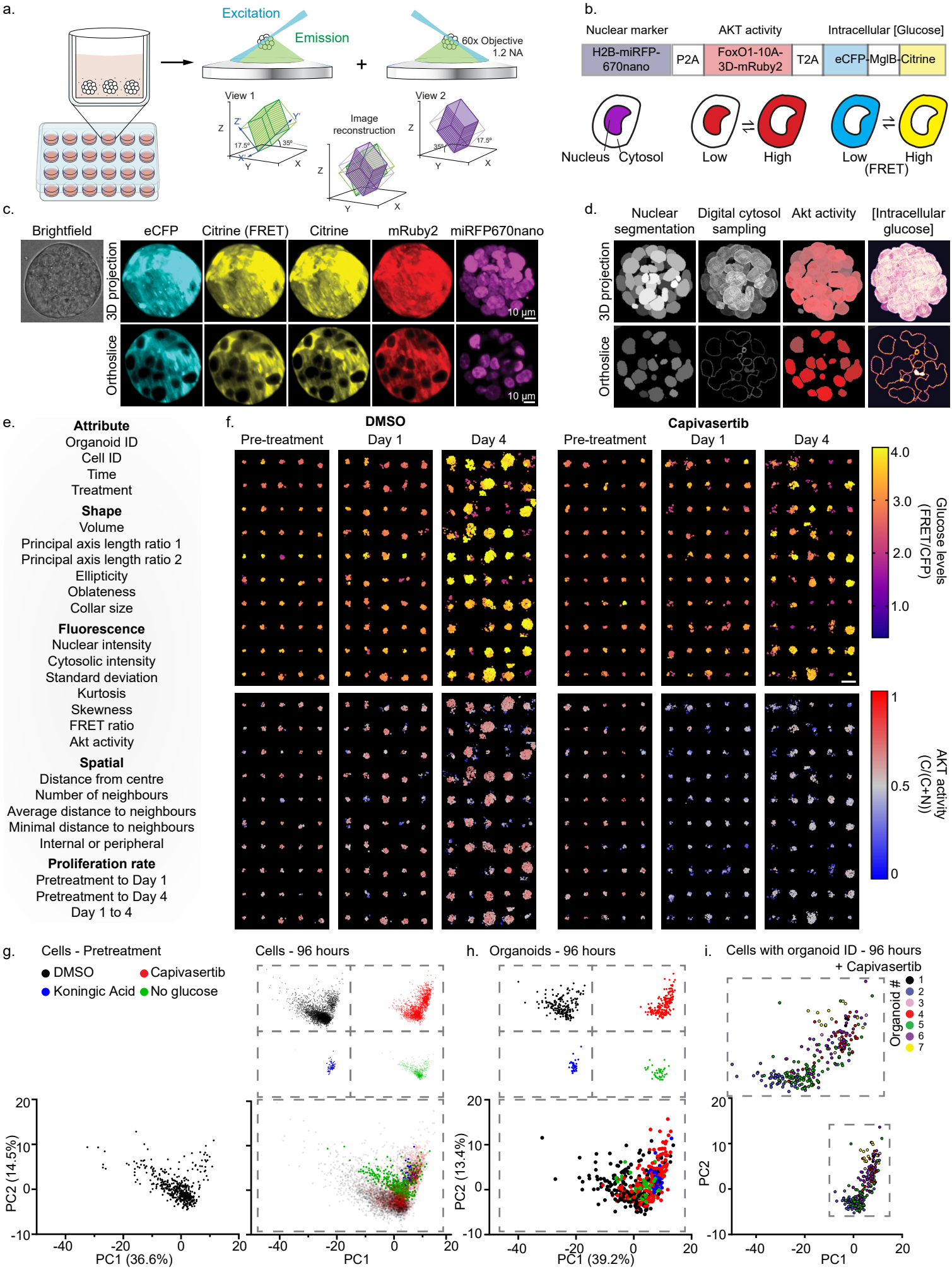
a.
Excitation
Emission
60x Objective
1.2 NA
View 1
View 2
Image reconstruction
b.
Nuclear marker
AKT activity
Intracellular [Glucose]
H2B-miRFP-670nano
P2A
FoxO1-10A-3D-mRuby2
T2A
eCFP
MglB
Citrine
Nucleus
Cytosol
Low
High
Low
High
(FRET)
c.
Brightfield
eCFP
Citrine (FRET)
Citrine
mRuby2
miRFP670nano
3D projection
Orthoslice
10 µm
d.
Nuclear segmentation
Digital cytosol sampling
Akt activity
[Intracellular glucose]
3D projection
Orthoslice
e.
Attribute
Organoid ID
Cell ID
Time
Treatment
Shape
Volume
Principal axis length ratio 1
Principal axis length ratio 2
Ellipticity
Oblateness
Collar size
Fluorescence
Nuclear intensity
Cytosolic intensity
Standard deviation
Kurtosis
Skewness
FRET ratio
Akt activity
Spatial
Distance from centre
Number of neighbours
Average distance to neighbours
Minimal distance to neighbours
Internal or peripheral
Proliferation rate
Pretreatment to Day 1
Pretreatment to Day 4
Day 1 to 4
f.
DMSO
Capivasertib
Pre-treatment
Day 1
Day 4
Pre-treatment
Day 1
Day 4
4.0
3.0
2.0
1.0
Glucose levels (FRET/CFP)
1
0.5
0
AKT activity (C/(C+N))
g.
Cells - Pretreatment
DMSO
Capivasertib
Koningic Acid
No glucose
Cells - 96 hours
PC2 (14.5%)
PC1 (36.6%)
PC1
h.
Organoids - 96 hours
PC2 (13.4%)
PC1 (39.2%)
i.
Cells with organoid ID - 96 hours
+ Capivasertib
Organoid #
1
2
3
4
5
6
7
PC2
PC1

Figure 3.

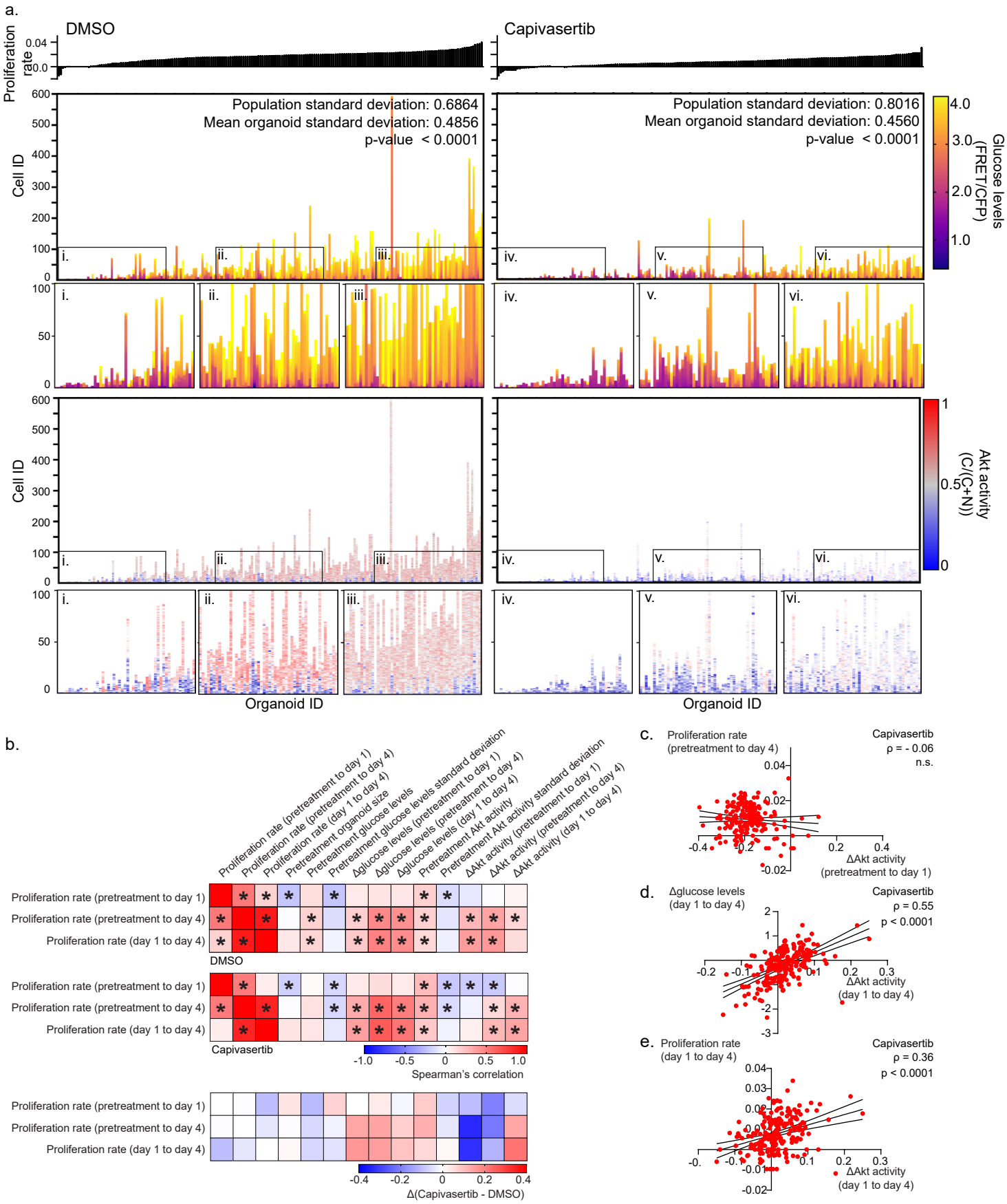
a.
DMSO
Capivasertib
Proliferation rate
Population standard deviation: 0.6864
Mean organoid standard deviation: 0.4856
p-value < 0.0001
Population standard deviation: 0.8016
Mean organoid standard deviation: 0.4560
p-value < 0.0001
Cell ID
Glucose levels (FRET/CFP)
Akt activity (C/(C+N))
Organoid ID
b.
Proliferation rate (pretreatment to day 1)
Proliferation rate (pretreatment to day 4)
Proliferation rate (day 1 to day 4)
Pretreatment organoid size
Pretreatment glucose levels
Δglucose levels standard deviation
Δglucose levels (pretreatment to day 1)
Δglucose levels (pretreatment to day 4)
Δglucose levels (day 1 to day 4)
Pretreatment Akt activity
Pretreatment Akt activity standard deviation
ΔAkt activity (pretreatment to day 1)
ΔAkt activity (pretreatment to day 4)
ΔAkt activity (day 1 to day 4)
DMSO
Capivasertib
Spearman's correlation
Δ(Capivasertib - DMSO)
c.
Proliferation rate (pretreatment to day 4)
Capivasertib
ρ = - 0.06
n.s.
ΔAkt activity (pretreatment to day 1)
d.
Δglucose levels (day 1 to day 4)
Capivasertib
ρ = 0.55
p < 0.0001
ΔAkt activity (day 1 to day 4)
e.
Proliferation rate (day 1 to day 4)
Capivasertib
ρ = 0.36
p < 0.0001
ΔAkt activity (day 1 to day 4)

Figure 4.

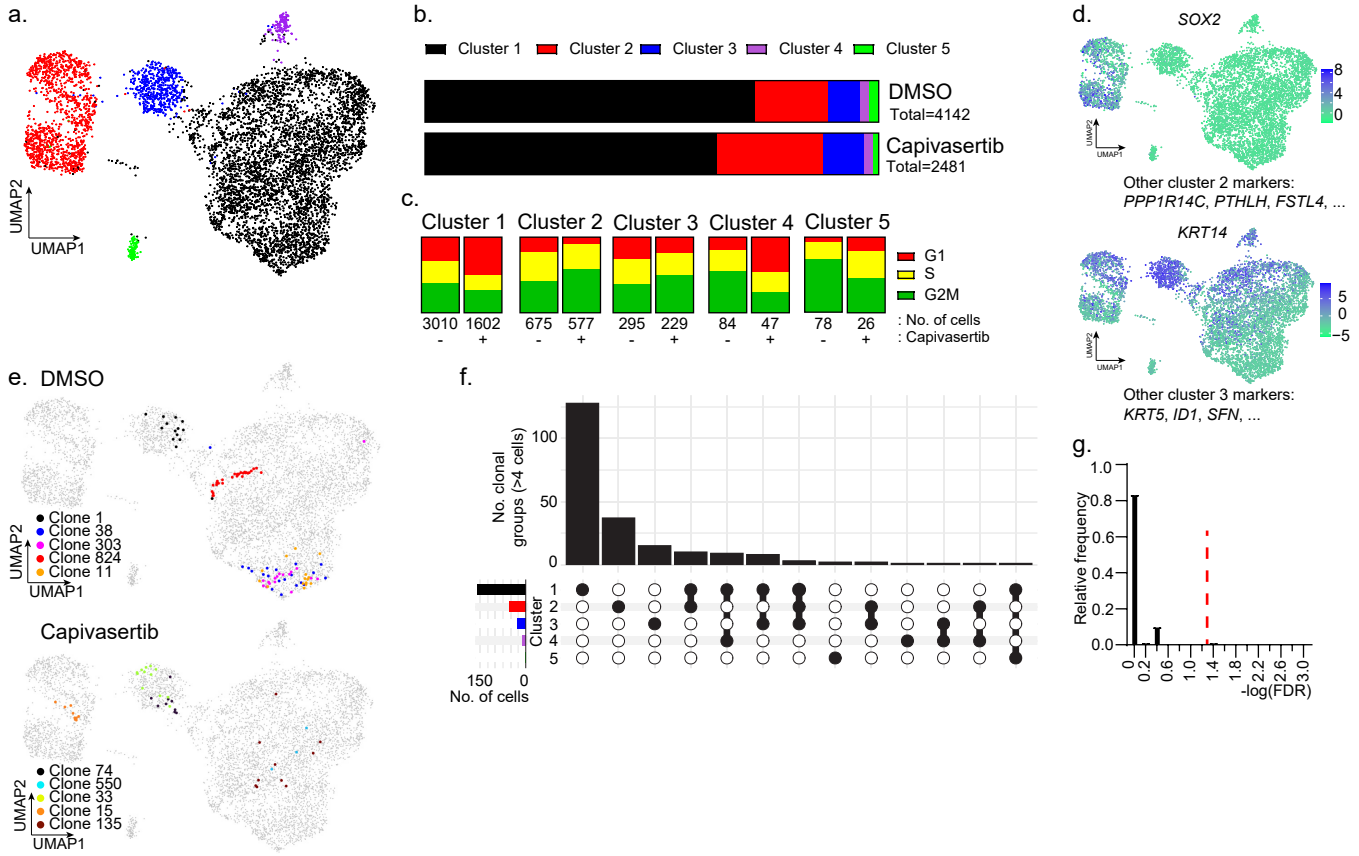
a.
UMAP2
UMAP1
b.
Cluster 1
Cluster 2
Cluster 3
Cluster 4
Cluster 5
DMSO
Total=4142
Capivasertib
Total=2481
c.
Cluster 1
Cluster 2
Cluster 3
Cluster 4
Cluster 5
G1
S
G2M
3010 1602 675 577 295 229 84 47 78 26
- + - + - + - + - +
: No. of cells
: Capivasertib
d.
SOX2
8
4
0
Other cluster 2 markers:
PPP1R14C, PTHLH, FSTL4, ...
KRT14
5
0
−5
Other cluster 3 markers:
KRT5, ID1, SFN, ...
e. DMSO
Clone 1
Clone 38
Clone 303
Clone 824
Clone 11
Capivasertib
Clone 74
Clone 550
Clone 33
Clone 15
Clone 135
f.
No. clonal groups (>4 cells)
100
50
0
Cluster
1
2
3
4
5
150
0
No. of cells
g.
Relative frequency
1.0
0.8
0.6
0.4
0.2
0.0
0
0.2
0.6
1.0
1.4
1.8
2.2
2.6
3.0
-log(FDR)

Figure 5.

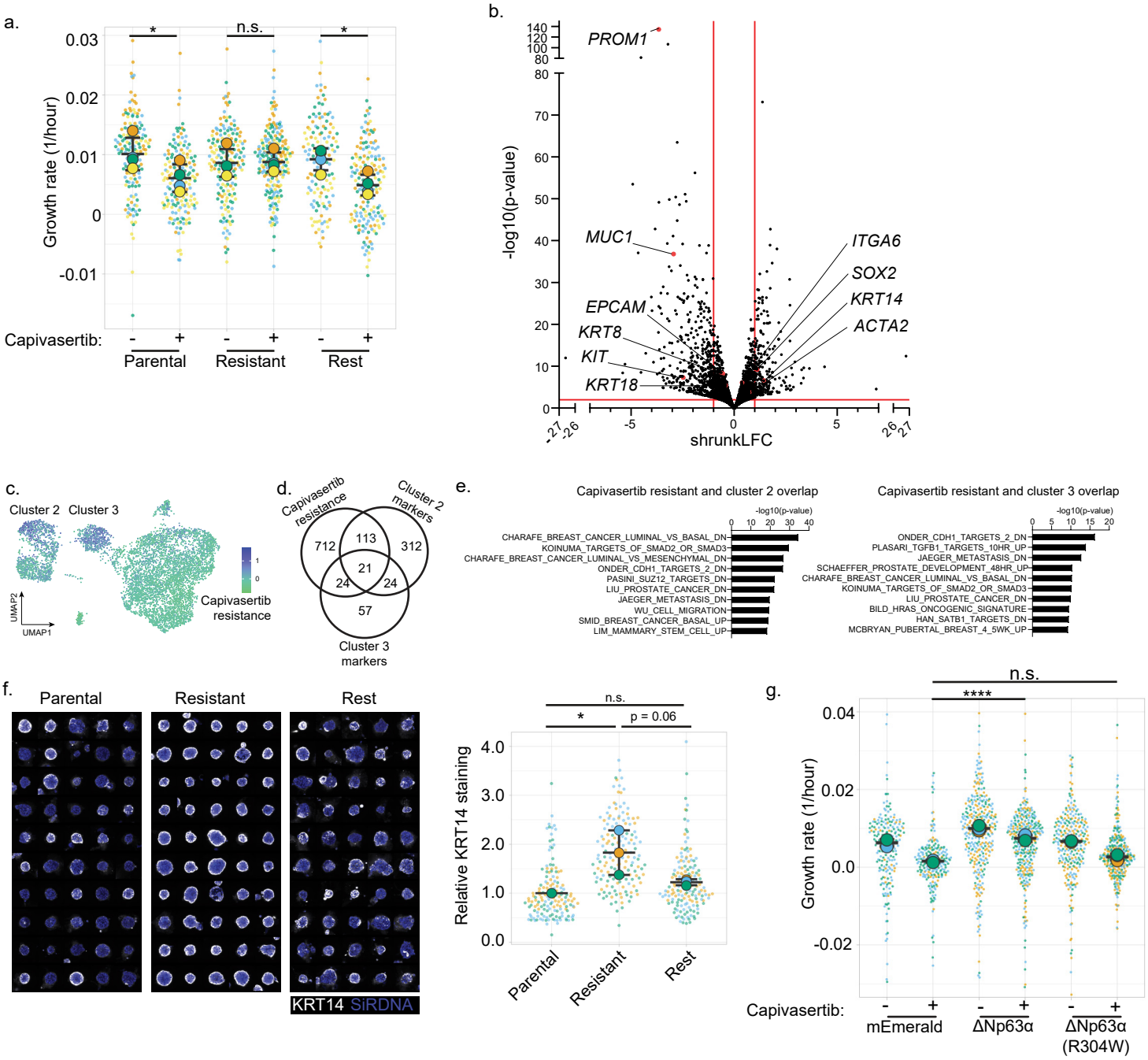
a.
Growth rate (1/hour)
Capivasertib:
Parental
Resistant
Rest
n.s.
b.
-log10(p-value)
shrunkLFC
PROM1
MUC1
EPCAM
KRT8
KIT
KRT18
ITGA6
SOX2
KRT14
ACTA2
c.
Cluster 2
Cluster 3
UMAP1
UMAP2
Capivasertib resistance
d.
Capivasertib resistance
Cluster 2 markers
Cluster 3 markers
712
113
312
21
24
24
57
e.
Capivasertib resistant and cluster 2 overlap
Capivasertib resistant and cluster 3 overlap
-log10(p-value)
CHARAFE_BREAST_CANCER_LUMINAL_VS_BASAL_DN
KOINUMA_TARGETS_OF_SMAD2_OR_SMAD3
CHARAFE_BREAST_CANCER_LUMINAL_VS_MESENCHYMAL_DN
ONDER_CDH1_TARGETS_2_DN
PASINI_SUZ12_TARGETS_DN
LIU_PROSTATE_CANCER_DN
JAEGER_METASTASIS_DN
WU_CELL_MIGRATION
SMID_BREAST_CANCER_BASAL_UP
LIM_MAMMARY_STEM_CELL_UP
ONDER_CDH1_TARGETS_2_DN
PLASARI_TGFB1_TARGETS_10HR_UP
JAEGER_METASTASIS_DN
SCHAEFFER_PROSTATE_DEVELOPMENT_48HR_UP
CHARAFE_BREAST_CANCER_LUMINAL_VS_BASAL_DN
KOINUMA_TARGETS_OF_SMAD2_OR_SMAD3
LIU_PROSTATE_CANCER_DN
BILD_HRAS_ONCOGENIC_SIGNATURE
HAN_SATB1_TARGETS_DN
MCBRYAN_PUBERTAL_BREAST_4_5WK_UP
f.
Parental
Resistant
Rest
KRT14 SiRDNA
Relative KRT14 staining
n.s.
*
p = 0.06
g.
Growth rate (1/hour)
n.s.
****
Capivasertib:
mEmerald
ΔNp63α
ΔNp63α (R304W)

Figure 6.

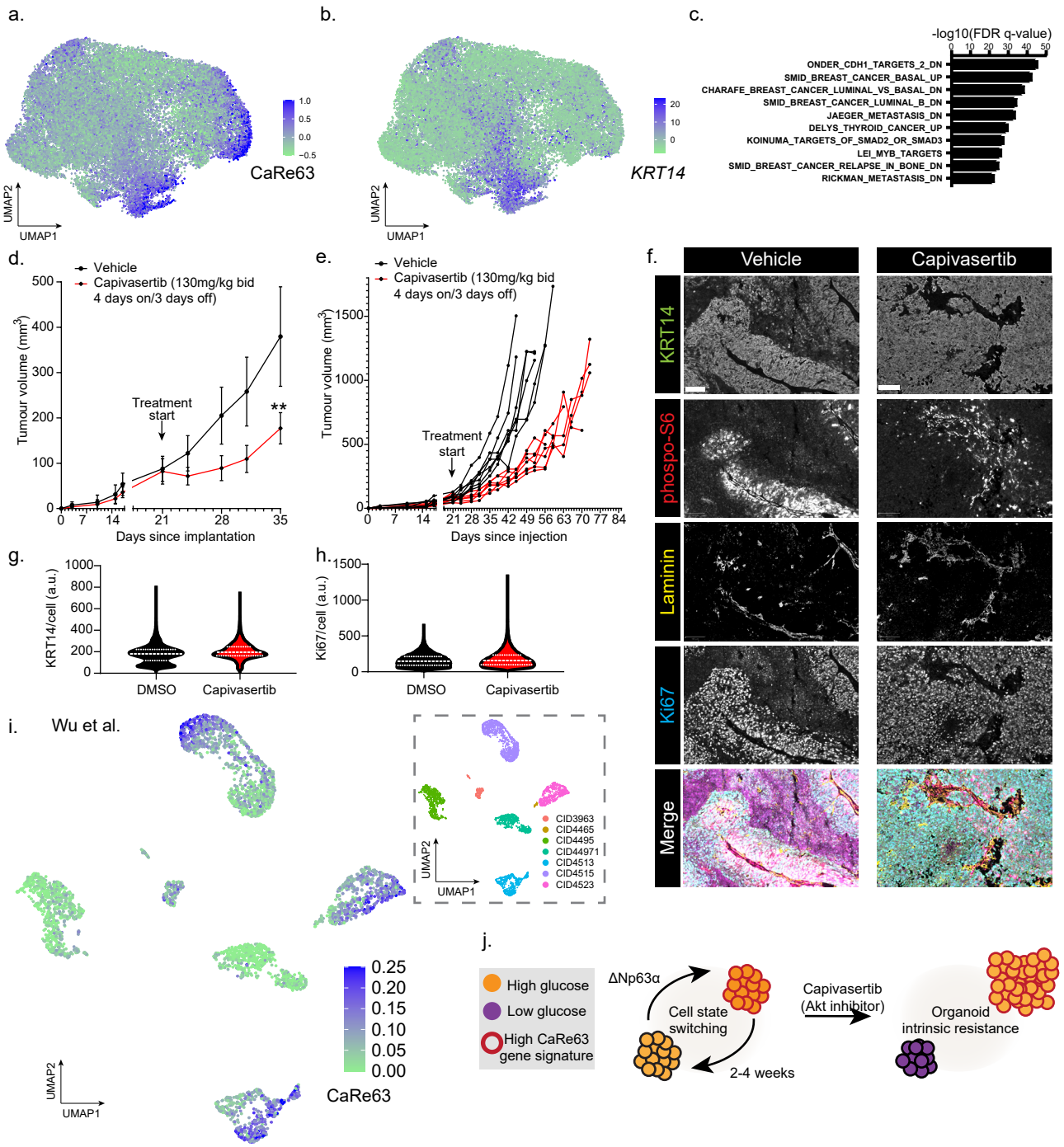
a.
CaRe63
UMAP2
UMAP1
b.
KRT14
c.
-log10(FDR q-value)
ONDER_CDH1_TARGETS_2_DN
SMID_BREAST_CANCER_BASAL_UP
CHARAFE_BREAST_CANCER_LUMINAL_VS_BASAL_DN
SMID_BREAST_CANCER_LUMINAL_B_DN
JAEGER_METASTASIS_DN
DELYS_THYROID_CANCER_UP
KOINUMA_TARGETS_OF_SMAD2_OR_SMAD3
LEI_MYB_TARGETS
SMID_BREAST_CANCER_RELAPSE_IN_BONE_DN
RICKMAN_METASTASIS_DN
d.
Vehicle
Capivasertib (130mg/kg bid 4 days on/3 days off)
Tumour volume (mm3)
Treatment start
Days since implantation
e.
Vehicle
Capivasertib (130mg/kg bid 4 days on/3 days off)
Tumour volume (mm3)
Treatment start
Days since injection
f.
Vehicle
Capivasertib
KRT14
phospo-S6
Laminin
Ki67
Merge
g.
KRT14/cell (a.u.)
DMSO
Capivasertib
h.
Ki67/cell (a.u.)
DMSO
Capivasertib
i.
Wu et al.
CID3963
CID4465
CID4495
CID44971
CID4513
CID4515
CID4523
CaRe63
j.
High glucose
Low glucose
High CaRe63 gene signature
ΔNp63α
Cell state switching
2-4 weeks
Capivasertib (Akt inhibitor)
Organoid intrinsic resistance

Supplemental Figure 1.

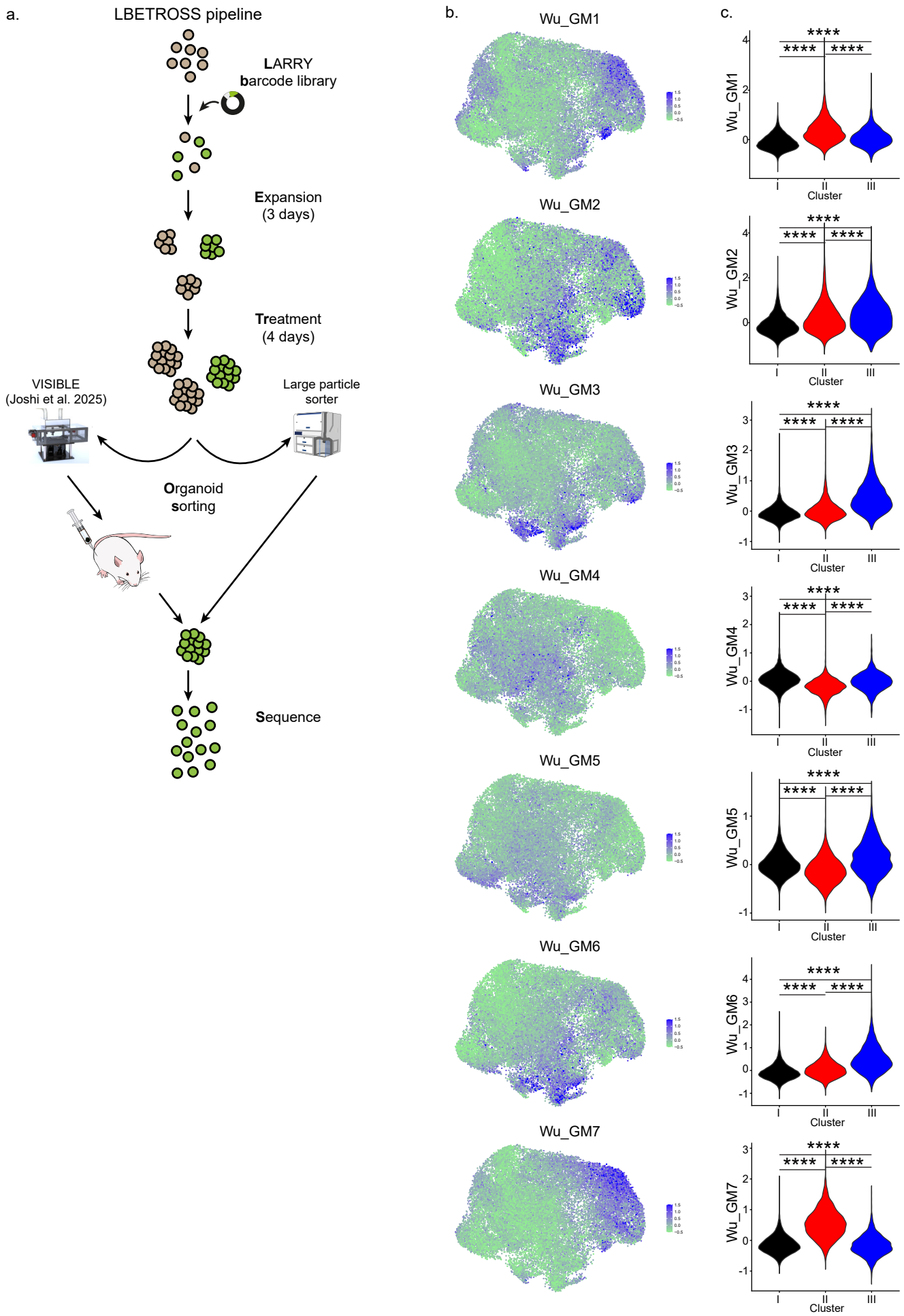

Supplemental Figure 2.

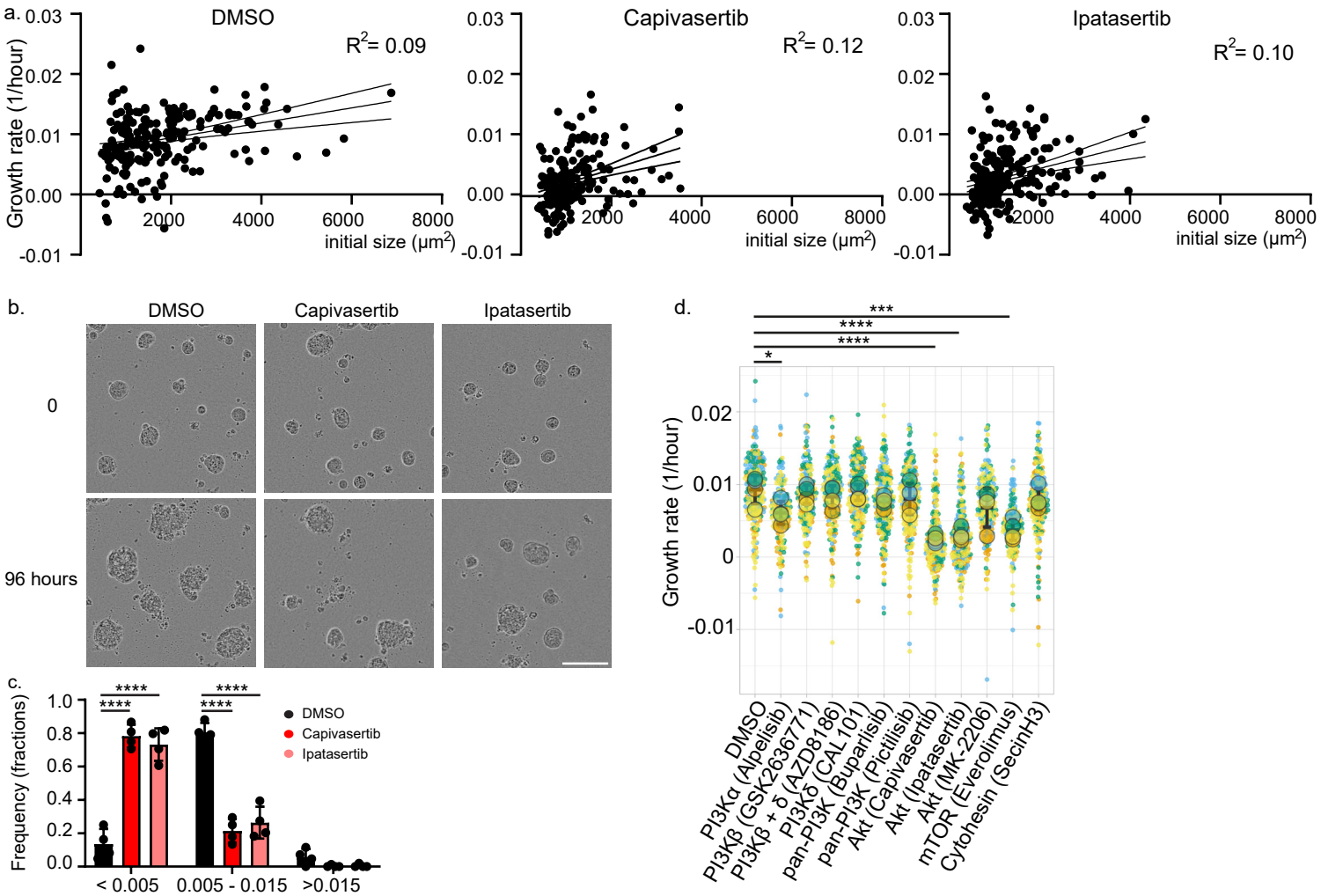

Supplemental Figure 3

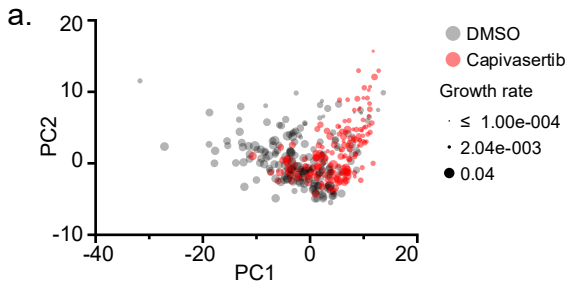

Supplemental Figure 4

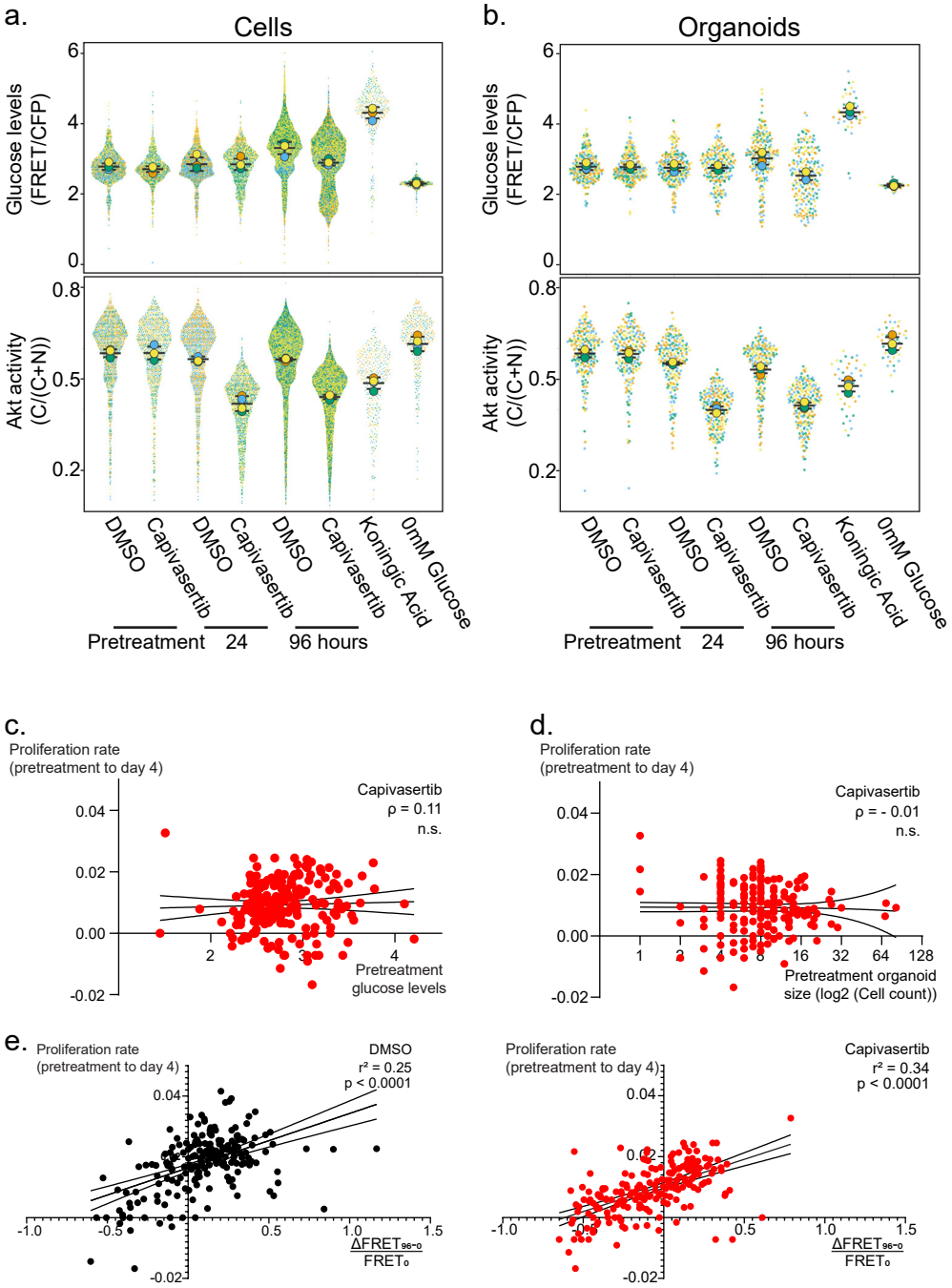

Supplemental Figure 5.

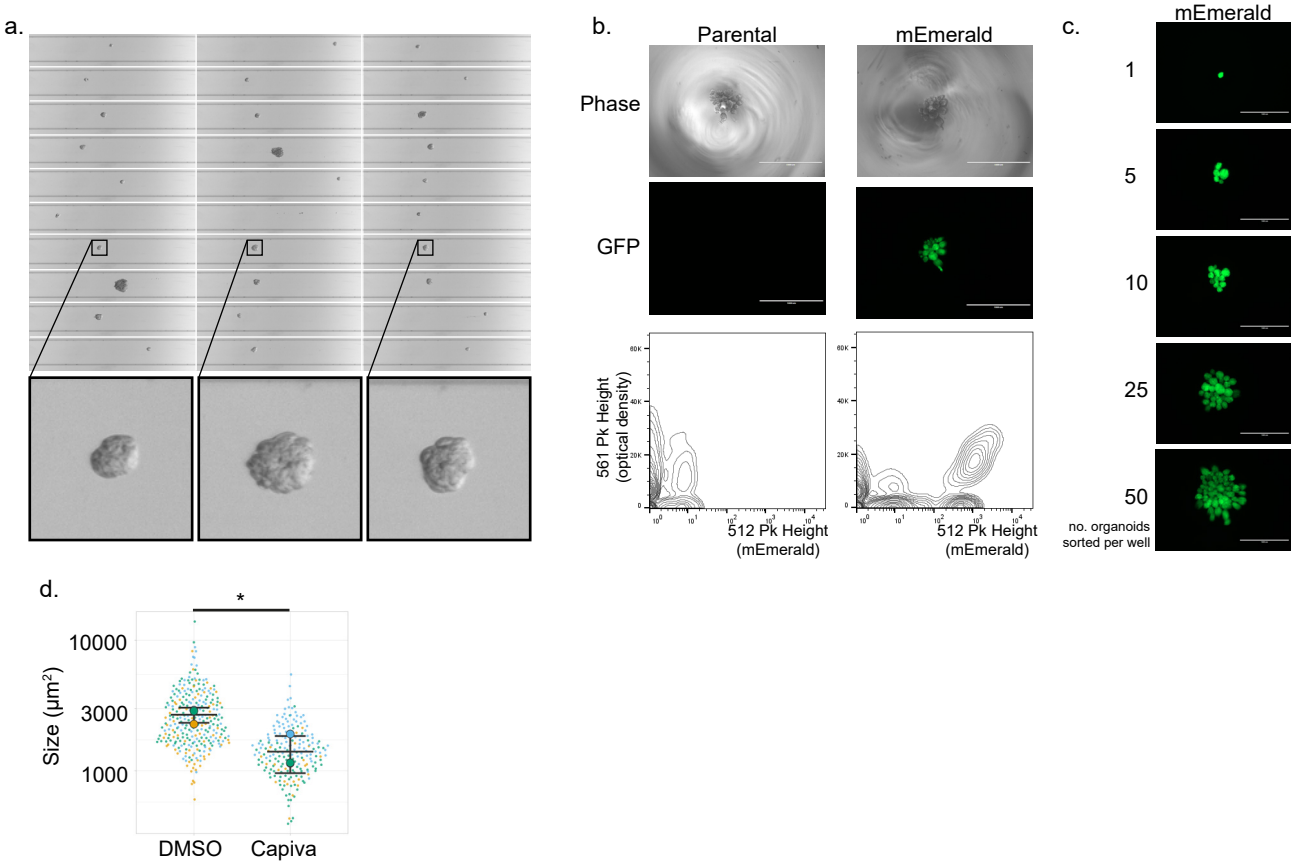

Supplemental Figure 6. Metabolomic analysis of Capivasertib resistant organoids

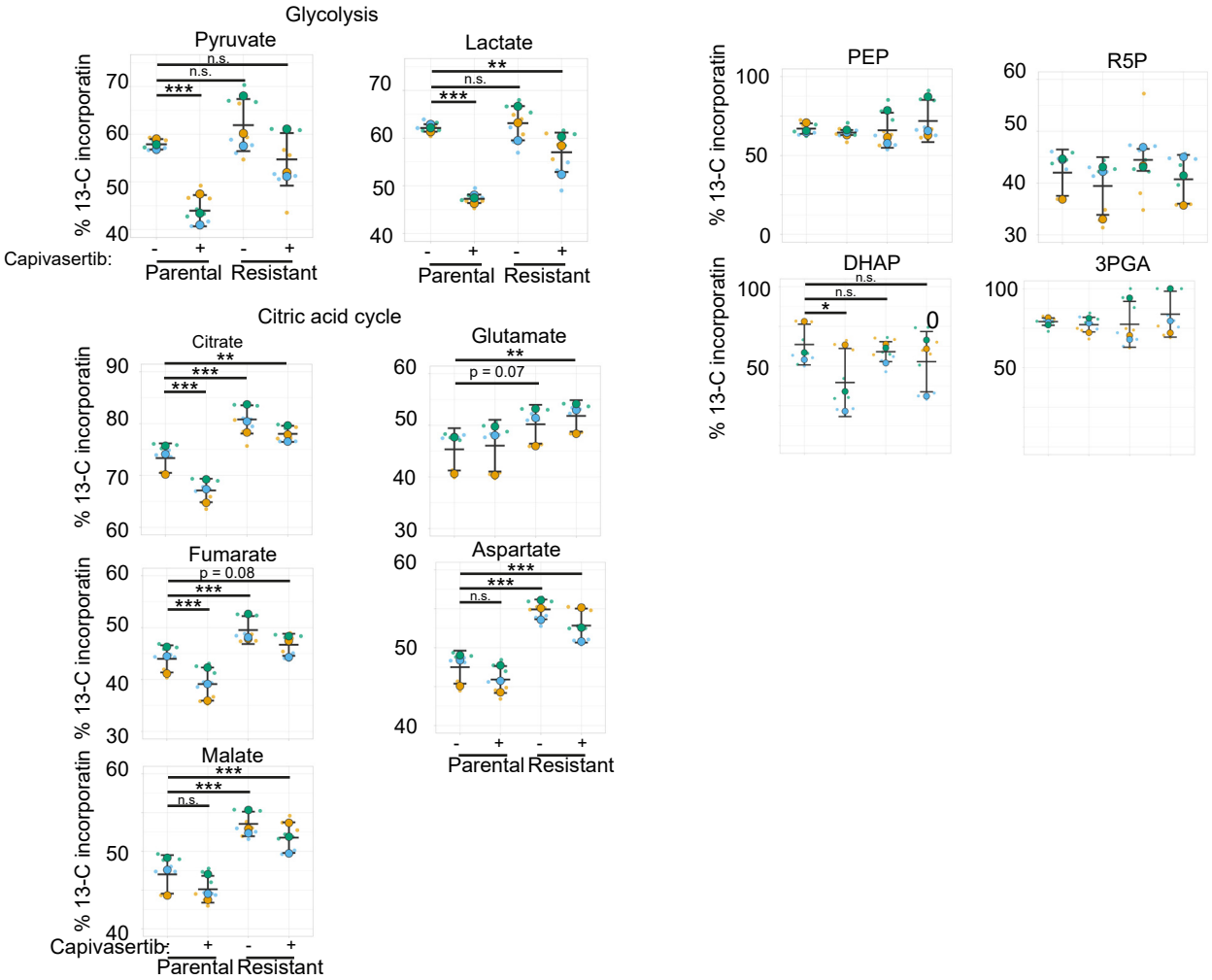
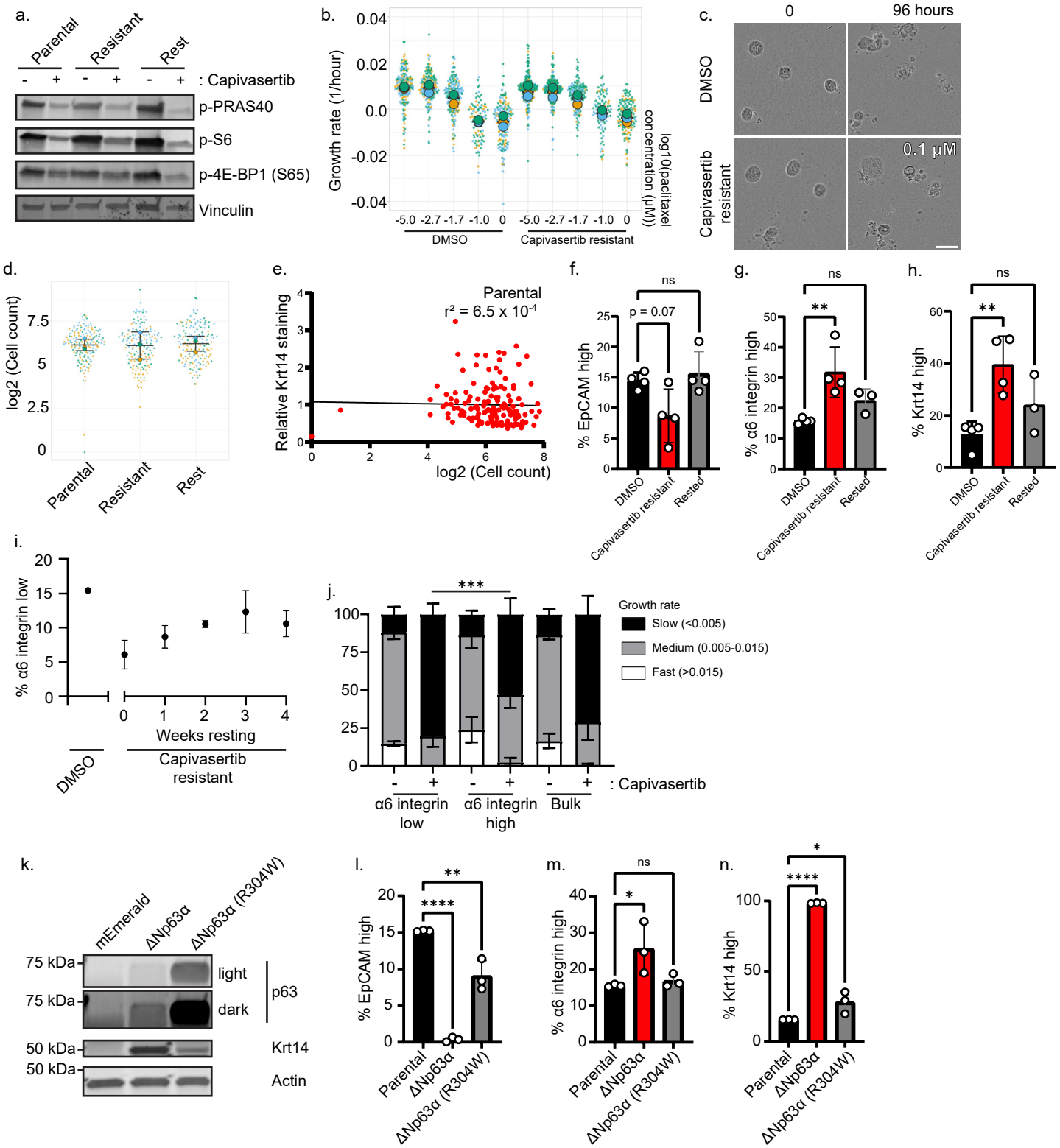
Supplemental Figure 7.